Cell Reports

Article

Degradation of CCNK/CDK12 is a druggable vulnerability of colorectal cancer

Graphical abstract

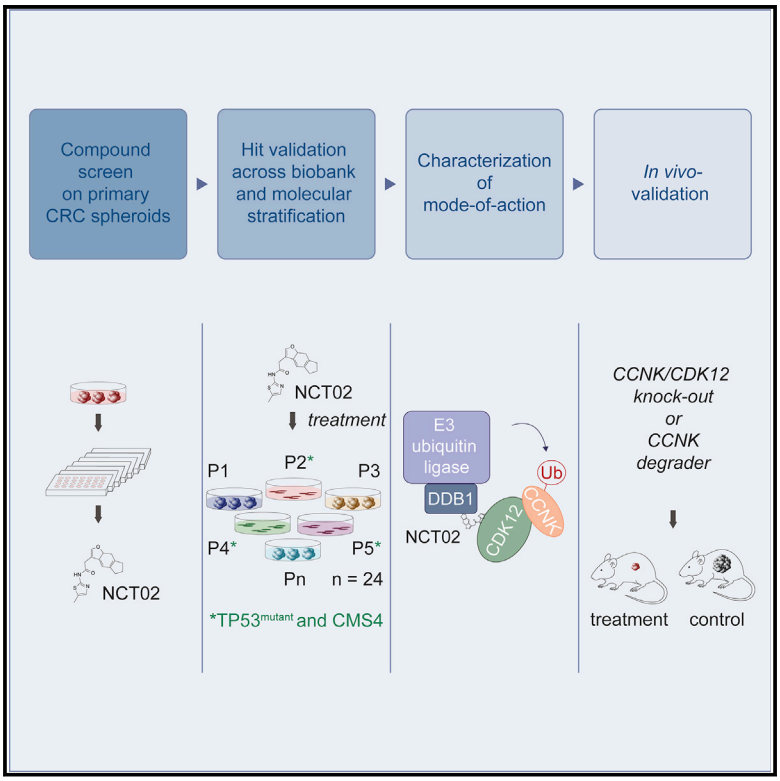

Authors

Sebastian M. Dieter, Christine Siegl, Paula L. Codó, ..., Martin Lange, Friederike Herbst, Hanno Glimm

Correspondence

sebastian.dieter@nct-heidelberg.de (S.M.D.),
hanno.glimm@nct-dresden.de (H.G.)

In brief

Dieter et al. identify the compound NCT02 as inhibitor of patient-derived colorectal cancer cell viability. They show that NCT02 acts as a molecular glue that induces CCNK ubiquitination and degradation. Targeted CCNK degradation is identified as a particular vulnerability of a subgroup of colorectal cancers that can be exploited therapeutically.

Highlights

- A screen for inhibitory compounds of colorectal cancer spheroids identifies NCT02
- NCT02 acts as a molecular glue and induces degradation of CCNK and CDK12
- Knockout of CCNK or CDK12 and targeted CCNK degradation decrease tumor growth
- TP53 deficiency and consensus molecular subtype 4 predict sensitivity to NCT02

Dieter et al., 2021, Cell Reports *36*, 109394
July 20, 2021
https://doi.org/10.1016/j.celrep.2021.109394

CellPress

Cell Reports

CellPress
OPEN ACCESS

Article

Degradation of CCNK/CDK12 is a druggable vulnerability of colorectal cancer

Sebastian M. Dieter,[1,2,*] Christine Siegl,[3,19] Paula L. Codó,[1,2,4,19] Mario Huerta,[1,2,19] Anna L. Ostermann-Parucha,[1,2] Erik Schulz,[5] Martina K. Zowada,[1,2,6] Sylvia Martin,[1,2] Karin Laaber,[1,2,6] Ali Nowrouzi,[7] Mona Blatter,[8,9] Sina Kreth,[8,9] Frank Westermann,[8,9] Axel Benner,[10] Ulrike Uhrig,[11] Kerstin Putzker,[11] Joe Lewis,[11] Andrea Haegebarth,[12] Dominik Mumberg,[12] Simon J. Holton,[12,13] Joerg Weiske,[12,13] Lena-Marit Toepper,[12,13] Ulrike Scheib,[12,13] Gerhard Siemeister,[12,13] Claudia R. Ball,[1,2,14,15] Bernhard Kuster,[16] Gabriele Stoehr,[17] Hannes Hahne,[17] Sarah Johannes,[18] Martin Lange,[12,13] Friederike Herbst,[1,2] and Hanno Glimm[1,2,14,15,20,*]

[1]Department of Translational Medical Oncology, National Center for Tumor Diseases (NCT) Dresden and German Cancer Research Center (DKFZ), 01307 Dresden, Germany
[2]Translational Functional Cancer Genomics, NCT and DKFZ Heidelberg, 69120 Heidelberg, Germany
[3]Merck KGaA, 64293 Darmstadt, Germany
[4]CureVac AG, 60325 Frankfurt am Main, Germany
[5]Department of General, Visceral and Transplantation Surgery, Heidelberg University Hospital, 69120 Heidelberg, Germany
[6]Faculty of Biosciences, Heidelberg University, 69120 Heidelberg, Germany
[7]Division of Molecular and Translational Radiation Oncology, Heidelberg Medical Faculty, Heidelberg University, 69120 Heidelberg, Germany
[8]Hopp Children's Cancer Center Heidelberg (KiTZ), 69120 Heidelberg, Germany
[9]Division of Neuroblastoma Genomics, DKFZ Heidelberg, 69120 Heidelberg, Germany
[10]Division of Biostatistics, DKFZ Heidelberg, 69120 Heidelberg, Germany
[11]European Molecular Biology Laboratory (EMBL), Chemical Biology Core Facility, 69117 Heidelberg, Germany
[12]Bayer AG, Research & Development, Pharmaceuticals, 13353 Berlin, Germany
[13]Nuvisan Innovation Campus Berlin GmbH, 13353 Berlin, Germany
[14]German Cancer Consortium (DKTK), 01307 Dresden, Germany
[15]Center for Personalized Oncology, University Hospital Carl Gustav Carus Dresden at TU Dresden, 01307 Dresden, Germany
[16]Chair of Proteomics and Bioanalytics, Technical University of Munich, 85354 Freising, Germany
[17]OmicScouts GmbH, 85354 Freising, Germany
[18]Bayer AG, Research & Development, Pharmaceuticals, 42117 Wuppertal, Germany
[19]These authors contributed equally
[20]Lead contact
*Correspondence: sebastian.dieter@nct-heidelberg.de (S.M.D.), hanno.glimm@nct-dresden.de (H.G.)
https://doi.org/10.1016/j.celrep.2021.109394

SUMMARY

Novel treatment options for metastatic colorectal cancer (CRC) are urgently needed to improve patient outcome. Here, we screen a library of non-characterized small molecules against a heterogeneous collection of patient-derived CRC spheroids. By prioritizing compounds with inhibitory activity in a subset of—but not all—spheroid cultures, NCT02 is identified as a candidate with minimal risk of non-specific toxicity. Mechanistically, we show that NCT02 acts as molecular glue that induces ubiquitination of cyclin K (CCNK) and proteasomal degradation of CCNK and its complex partner CDK12. Knockout of CCNK or CDK12 decreases proliferation of CRC cells *in vitro* and tumor growth *in vivo*. Interestingly, sensitivity to pharmacological CCNK/CDK12 degradation is associated with TP53 deficiency and consensus molecular subtype 4 *in vitro* and in patient-derived xenografts. We thus demonstrate the efficacy of targeted CCNK/CDK12 degradation for a CRC subset, highlighting the potential of drug-induced proteolysis for difficult-to-treat types of cancer.

INTRODUCTION

The response of a malignant tumor to drug treatment can be significantly mitigated by cellular heterogeneity (Dagogo-Jack and Shaw, 2018). Genetically, individual tumors represent diverse assemblies of tumor cells with shared and unique molecular signatures, associated with different degrees of sensitivity to treatment. In addition, individual tumors across multiple tumor types including colorectal cancer (CRC) are built up as a functional hierarchy that comprises cell subfractions with substantial differences in self-renewal capacity and drug sensitivity (Prasetyanti and Medema, 2017). This functional hierarchy with stem-cell like tumor-initiating cells (TICs) at the apex is driven by epigenetic changes (e.g., chromatin methylation patterns), as well as paracrine interactions, and influenced by the cell-of-origin in which malignant transformation occurs (Bormann et al., 2018; Prasetyanti and Medema, 2017). Furthermore, functional heterogeneity of tumor cells is marked by considerable plasticity, which

hampers approaches aimed at eliminating distinct cellular subfractions that can be compensated by regeneration from alternative cell pools of the same tumor (Prasetyanti and Medema, 2017). The complexity that arises from this multi-faceted heterogeneity requires personalized and combinatorial treatment approaches, which is currently limited by the availability of compounds targeting patient-specific drivers or driver-associated dependencies (Shin et al., 2017). In consequence, there is a strong clinical need for novel compounds with defined activity in genetically and functionally characterized tumor cells.

Recent progress in developing more disease-relevant models (e.g., three-dimensional [3D] patient-derived cell culture systems) has stimulated increasing interest in phenotypic screens that—in contrast to target-based screens—filter compounds for modulating a phenotype of particular relevance for the disease of interest (e.g., induction of apoptosis in cancer cells) (Moffat et al., 2014). Notably, phenotypic screens can identify compounds that modulate targets that are not considered druggable—a prominent example being Lenalidomide that induces degradation of transcription factors that are critical drivers of multiple myeloma (Krönke et al., 2014). Still, identification of the molecular target and selection of a promising candidate from a list of toxic compounds remains a challenge for phenotypic screens (Eder et al., 2014).

3D patient-derived tumor models of CRC (i.e., organoid and spheroid cultures) allow maintenance and expansion of functionally relevant cell subfractions and harbor the patients' individual genetic lesions (Ishiguro et al., 2017; van de Wetering et al., 2015). These tumor cell models recapitulate the original patient tumor after transplantation into immunodeficient mice. Moreover, TICs that have the capacity to self-renew and maintain long-term tumor growth are usually rare within the tumor mass but highly enriched within spheroid cultures (Dieter et al., 2011; Ishiguro et al., 2017).

To identify novel compounds that are active against all functionally relevant CRC cell subfractions, we performed a compound screen using a library of ~80,000 non-characterized small molecules against primary CRC tumor spheroid culture (TSC) cells. Comprehensive transcriptomic and proteomic characterization of one inhibitory compound with selective activity in a subset of primary TSCs revealed molecular glue degradation as mechanism-of-action and identified a potential vulnerability of a subgroup of patients with CRC.

RESULTS

A collection of primary TSCs reflects CRC heterogeneity

As a platform for compound screening, we built up a biobank of 24 primary TSCs. TSCs were derived from primary and metastatic colorectal cancer samples and expanded for drug testing (Figure 1A; Table S1, patient characteristics). Two TSCs (TSC10T and TSC10L) were derived separately from the primary tumor and liver metastases of the same patient.

Whole-exome or whole-genome sequencing was performed to identify genetic aberrations present in individual TSCs (Figure 1B). The most commonly mutated genes in patients with CRC as identified by The Cancer Genome Atlas Network (Cancer Genome Atlas, 2012) were well represented in our biobank (Figure 1B).

Gene expression analysis of a large cohort of CRCs has revealed four consensus molecular subtypes (CMSs) with distinct biological features as well as differences in clinical outcome (Guinney et al., 2015). Transcriptome data were available for 21 TSCs, and all CMSs could be detected in our biobank (Figure 1B). In summary, our biobank of TSCs captured key aspects of the genomic and transcriptomic diversity of CRCs.

High-throughput screening identifies compounds with inhibitory activity against colorectal TSCs

To test whether TSCs can be reliably used for drug assays we first screened a library of ~4,000 compounds. TSC cells were treated with the compounds for 96 h, and viability was analyzed afterward using the ATPlite assay (Figures S1A and S1B). The *Z* factor score, a measure for the assay plate quality, was above 0.5 for all plates, indicating a robust assay. Thus, drug screening on primary TSCs was feasible.

For the final screen, a compound library of ~80,000 publicly available small molecules without known activity or interaction profile, assembled to cover a maximum of chemical diversity, was screened at 10 μM as in the pilot screen. Using a cut-off of 95% inhibition, 346 active compounds were identified (Figure 1C). Compounds were clustered into families based on structural similarity and prioritized by number of active family members, availability, and lack of interference with the ATPlite assay. Based on these criteria, 120 compounds were selected and re-tested on TSC03 in serial dilutions. Of the 120 tested compounds, 14 (NCT01–NCT14) (Figure 1D; Table S2) were chosen that showed an IC_{50} below 20 μM and appropriate dose-response curves (Hill slope between 0.5 and 2.5).

The compound NCT02 shows a selective response pattern

To further refine the selection and identify compounds with activity across different patient-derived TSCs while sparing non-malignant cells, these 14 compounds were tested against eight different TSCs and normal primary fibroblasts (Figure 1D). We were particularly interested in a compound that showed inhibitory activity in a subset of patient-derived TSCs rather than pan-inhibitory activity in order to minimize the risk of non-specific toxicity and increase the chance of establishing molecular markers predicting response to treatment. The compound that showed the most pronounced differential response profile and lacked activity against normal primary fibroblasts was NCT02 (Figure 1E). This compound represents a benzofurane derivative (Figure 1F). In biochemical interaction screens with 68 targets causing critical side-effects in patients and a collection of 468 kinases, NCT02 was largely inert, indicating that our selection strategy did not identify a promiscuous or non-specifically toxic compound (Table S3).

NCT02 inhibits self-renewing cells in genetically diverse colorectal TSCs

To determine the inhibitory activity of NCT02 across a larger set of genetically diverse TSCs, we performed viability assays on 24 patient-derived TSCs (Figure 2A). This confirmed the

CellPress
OPEN ACCESS

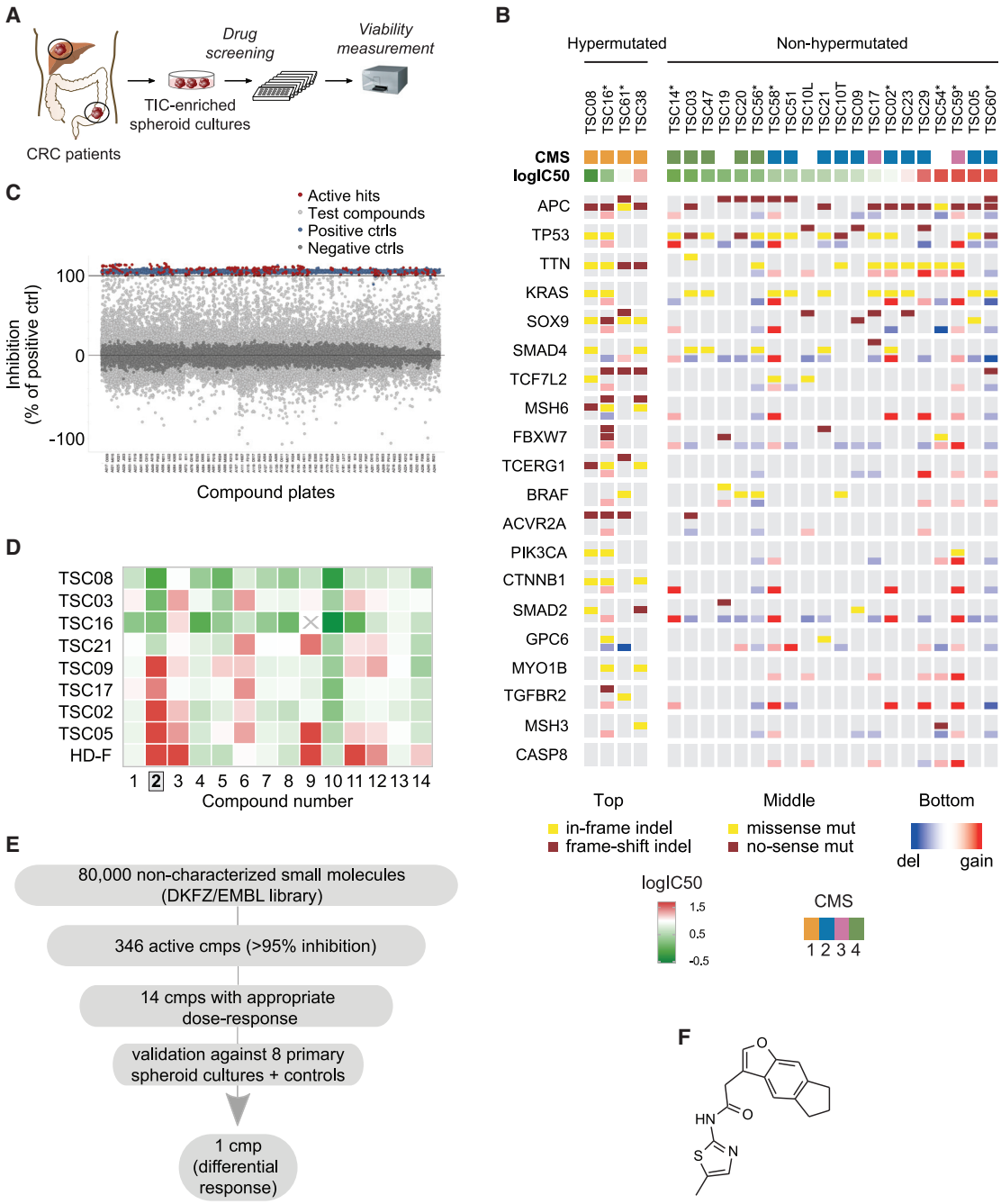

Figure 1. High-throughput screening identifies compounds with activity against primary TSCs

(A) A biobank of 24 primary TSCs was derived from primary and metastatic patients with CRC as a platform for compound screening.

(B) Whole-exome or whole-genome sequencing (the latter marked by asterisks) as well as transcriptome analysis of TSCs were performed to define the genetic make-up of individual TSCs and assign them to a CMS (missing boxes, no data available). Presented are the 20 genes most frequently affected by mutations (indel, insertion or deletion; mut, mutation; del, deletion). Sensitivity of TSCs is displayed as $\log IC_{50}$ (μM).

(C) A high-throughput compound screen against TSC03 was performed to identify novel compounds with inhibitory activity from a library of 80,000 non-characterized small molecules (ctrl, control).

(D) Validation of 14 inhibitory compounds from the primary screen against different TSCs and non-malignant primary human fibroblasts (HD-F; x = no data available; color scale for sensitivity [$\log IC_{50}$ μM] identical to B).

(E) Selection strategy for NCT02 from all active compounds (cmps) of the primary screen for further characterization.

(F) Chemical structure of the selected compound NCT02.

See also Figure S1 and Tables S1, S2, and S3.

heterogeneous response profile of NCT02 with 13 out of 24 TSCs being relatively sensitive (IC_{50} <4 μM), seven TSCs being resistant (IC_{50} >10 μM), and four TSCs displaying intermediate sensitivity (Table S1). As expected in primary cells, we detected some variability in viability assays for TSC02, TSC09, and TSC17, and multiple biological replicates finally revealed higher and consistent sensitivity of these TSCs toward NCT02 compared to initial measurements. In summary, NCT02 demonstrated activity on a broad range of genetically diverse CRC TSCs.

Due to the heterogeneous nature of our biobank of primary CRC TSCs, selection of TSCs suitable for individual validation experiments and secondary assays was necessary, which did not allow for consistently using the same set of TSCs. To assess the inhibitory activity of NCT02 against the self-renewing spheroid-forming cell (SFC) subfraction, generally regarded as *in vitro* surrogate for TICs (Ricci-Vitiani et al., 2007), five sensitive TSCs were treated with increasing concentrations of NCT02 or DMSO. Single cells were sorted into 96-well plates, monitored for up to 21 days, and the number of wells with emerging spheroids was quantified. Treatment with NCT02 decreased the frequency of SFCs in a concentration-dependent manner, indicating inhibitory activity of NCT02 against self-renewing SFCs (Figure 2B).

NCT02 induces apoptosis

Inhibitory activity of a drug can be mediated by various mechanisms including cell-cycle arrest or cell death. We first analyzed the cell-cycle activity of TSCs after treatment with NCT02 (Figure 2C) but did not observe a substantial and consistent accumulation of cells in any of the cell-cycle phases, arguing against cell-cycle arrest as mechanism of inhibition. In contrast, we detected a concentration-dependent increase in the percentage of cleaved PARP (cPARP)-positive cells in four out of five sensitive TSCs after treatment with NCT02, indicating that induction of apoptosis contributed to inhibition of sensitive TSCs by NCT02 (Figure 2D).

NCT02 interferes with the DNA damage response

To gain insights into pathways that were affected by treatment with NCT02, transcriptome analysis of TSC cells after 12 h of treatment was performed (Figure 3A; Table S4). Differentially expressed genes were used to perform Ingenuity pathway analysis, which revealed 37 pathways significantly deregulated in sensitive TSC cells after treatment. Strikingly, the most significantly deregulated pathways comprised numerous pathways associated with DNA damage repair (Figure 3B; Table S4). The downregulation of individual genes of these DNA damage response pathways after treatment with NCT02 was confirmed by qPCR (Figure 3C). Many downregulated genes were implicated in DNA double strand break (DSB) repair. Downregulation of ATM and RAD51—both involved in sensing and repair of DSBs—was also confirmed on protein level (Figure S1C). Moreover, we assessed phospho-Ser139-H2AX (γH2AX) levels as a marker for DSBs and genomic instability by flow cytometry, which revealed an enrichment of γH2AX-positive cells after treatment with NCT02 (Figure 3D). Thus, NCT02 induced the downregulation of genes involved in DNA damage repair, which was associated with an increase in unrepaired DSBs and genomic instability.

Ingenuity upstream regulator analysis identified several transcriptional regulators potentially inhibited by NCT02, of which cyclin K (CCNK) showed both the lowest p value ($p = 9.22 \times 10^{-8}$) and the highest *Z* score for inhibition (−3.65) (Figure 3E). Cyclin-dependent kinase 12 (CDK12), which forms a complex with CCNK to function as a transcriptional regulator of DNA damage repair genes, was additionally identified as one of the top hits (Table S4).

Thermal proteome profiling identifies CDK12 as a potential target of NCT02

In a complementary approach to identify molecular targets of NCT02, thermal proteome profiling (TPP) was performed (Figure 4A) (Savitski et al., 2014). This assay is based on the concept that binding of a compound to a protein can result in thermal stabilization of the protein and—consequently—in a detectable shift of its melting curve. This allows for assessing ligand binding in living cells without modification of the compound.

Thus, we treated sensitive TSC03 for 2 h with NCT02 or controls (an inactive derivative of NCT02 [$NCT02D^{inactive}$] and DMSO) (Figure S2A) and measured melting curves of more than 5,000 proteins in all conditions using quantitative mass spectrometry. We identified 43 proteins with significantly differing melting curves, of which 15 proteins showed a shift toward increased stability, and 28 proteins showed a shift toward decreased stability (Figure 4B; Table S5). Interestingly, CDK12 that—together with its complex partner CCNK—has been identified by gene expression analysis as a potential upstream regulator inhibited by NCT02 was among the proteins with the strongest and most significant shifts in thermal stability. Unexpectedly, the thermal shift of CDK12 resulted in a lower melting point reflecting decreased thermal stability upon cell treatment (Figure 4C). Moreover, its complex partner CCNK was identified by mass spectrometry only in cells treated with $NCT02D^{inactive}$ and DMSO, but not NCT02.

We thus hypothesized that complex formation of CCNK and CDK12, which contributes to stability of both complex partners (Barette et al., 2001), might have been disturbed by NCT02. In this case, both proteins—even if bound by NCT02—would be destabilized, which could be reflected by decreased thermal stability (CDK12) or decreased protein abundance (CCNK).

Chemical proteomics identify CCNK and CDK12 as targets of NCT02

Because TPP of living cells cannot readily distinguish between direct compound targets and downstream effects, we performed compound pull-down assays and quantitative mass spectrometry to identify proteins bound by NCT02. For this purpose, a derivative of NCT02 ($NCT02D^{active}$) (Figure S2B) was coupled to Sepharose beads and used to pull-down proteins from TSC03 cell extracts. NCT02D was selected, because it kept its activity in cellular assays with a highly correlating differential response profile across individual TSCs (Figures S2C and S2D), indicating that relevant target(s) of NCT02 were preserved. The experiments were performed with competitive treatment of living cells with 10 μM NCT02 or DMSO as control. When TSC03 cells were treated with NCT02 (10 μM, 2 h) followed by cell extraction and pull-down using immobilized $NCT02D^{active}$ as bait, we identified CCNK and CDK12 among the five

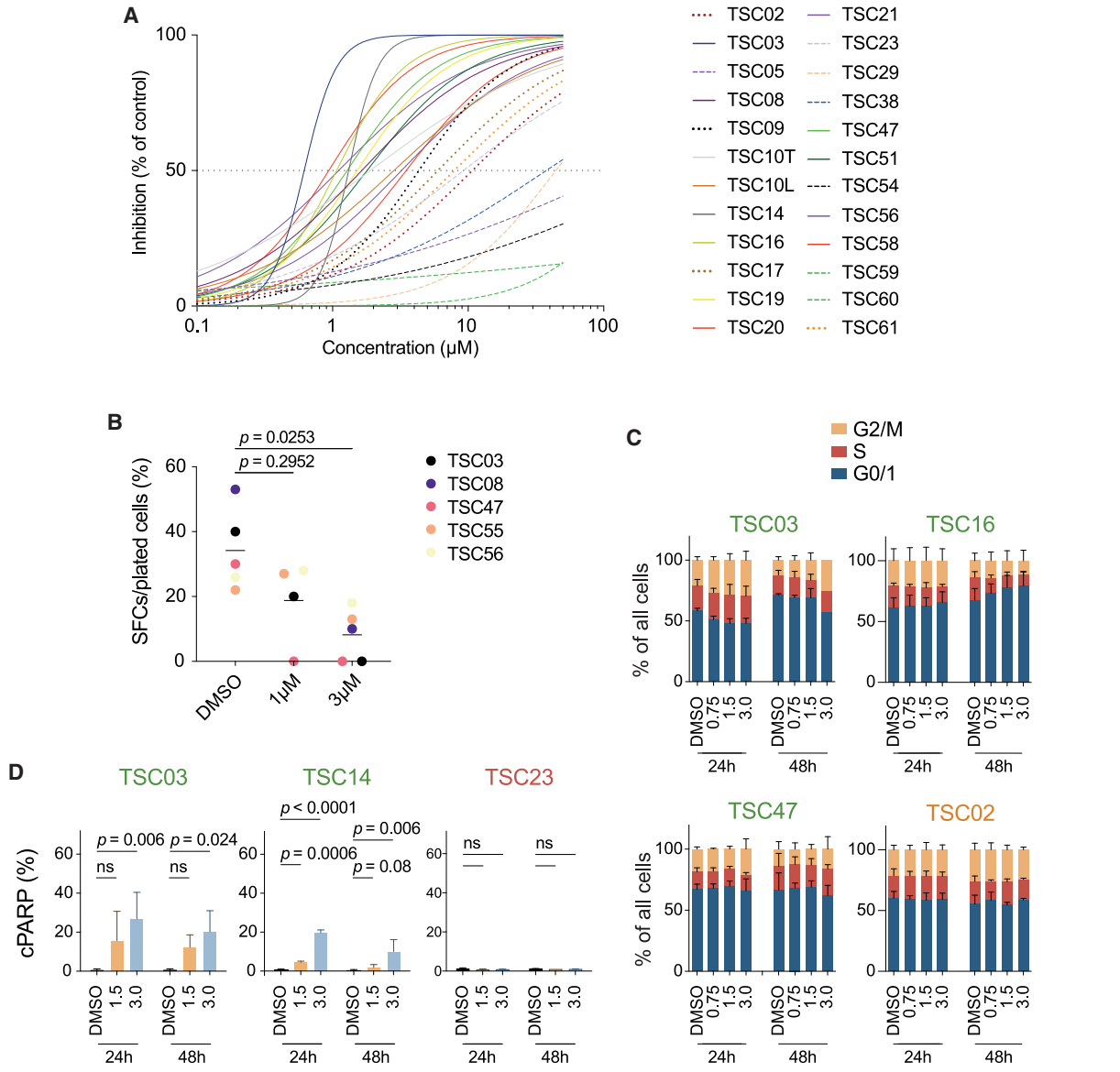

Figure 2. NCT02 inhibits self-renewing TSC cells and induces apoptosis

(A) Sensitivity of CRC TSCs to NCT02 was tested using viability assays (shown is one representative of at least three biological replicates per TSC [except for TSC60 and TSC61 with only one biological replicate]).

(B) TSC cells were treated with NCT02 for 19 h as indicated and seeded as single cells. The frequency of formed spheroids per number of seeded cells is shown (lines indicate mean; p values from unpaired, two-tailed t tests).

(C) Cell-cycle analysis of sensitive (green) and intermediate (orange) TSCs treated with NCT02 (concentrations in μM NCT02; presented are mean + SD of two biological replicates).

(D) Determination of cPARP^{+} cells after treatment of sensitive (green) and resistant (red) TSCs with NCT02 (concentrations in μM of NCT02; presented are mean + SD; p values from unpaired, two-tailed t tests; ns, not significant).

statistically significant proteins with the strongest reduction of protein intensity (Figures 4D and 4E; Table S5), either due to competitive binding by NCT02 or protein degradation. Interestingly, CDK13, an additional binding partner of CCNK and not detected in previous TPP experiments, was found with a significant reduction of protein intensity (although at low levels). Taken together, this indicates that CCNK/CDK12 and CCNK/CDK13 complexes are rather selectively affected by NCT02.

Because stable overexpression of CCNK or CDK12, respectively, could not be achieved, cells with combined overexpression of CCNK and CDK12 were generated (Figures S2E and S2F) and their sensitivity toward NCT02 was compared to control cells. Combined overexpression of CCNK/CDK12 decreased sensitivity toward NCT02, confirming the functional relevance of CCNK/CDK12 for the inhibitory effect of NCT02 (Figures 4F and 4G).

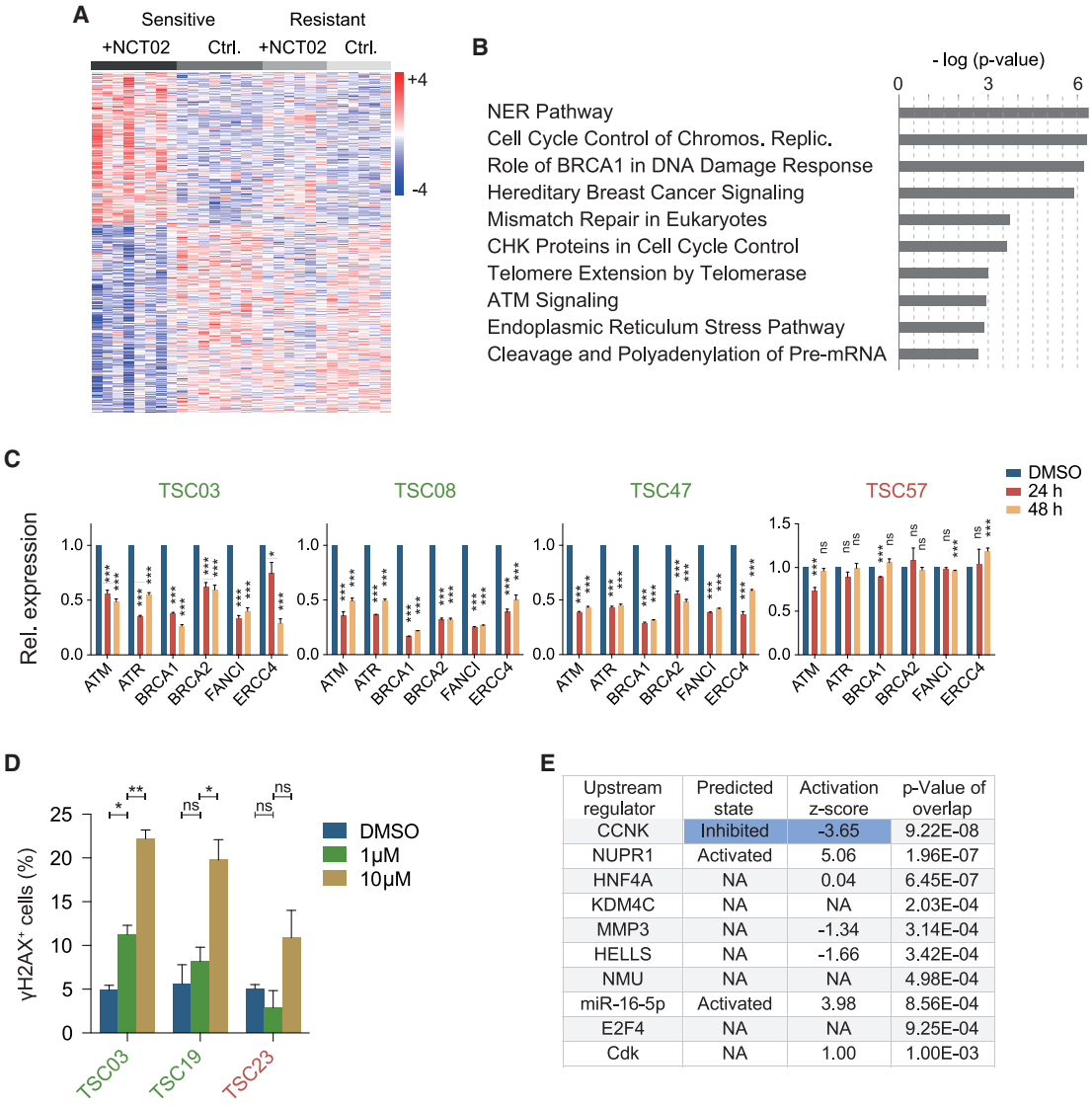

E

Upstream regulator	Predicted state	Activation z-score	p-Value of overlap
CCNK	Inhibited	-3.65	9.22E-08
NUPR1	Activated	5.06	1.96E-07
HNF4A	NA	0.04	6.45E-07
KDM4C	NA	NA	2.03E-04
MMP3	NA	-1.34	3.14E-04
HELLS	NA	-1.66	3.42E-04
NMU	NA	NA	4.98E-04
miR-16-5p	Activated	3.98	8.56E-04
E2F4	NA	NA	9.25E-04
Cdk	NA	1.00	1.00E-03

Figure 3. NCT02 interferes with the DNA damage response

(A) Differentially expressed genes after 12 h treatment with NCT02 (3 μM) or control (ctrl, DMSO; color scale indicates $\log_2$fold change; each column represents one TSC).

(B) Ingenuity pathway analysis showing most significantly affected pathways based on differentially expressed genes after treatment with NCT02.

(C) Validation of selected downregulated genes after treatment by qPCR (three technical replicates per TSC, normalized to GAPDH and DMSO; presented are mean ± SD; rel. expression, relative expression; p values from unpaired, two-tailed t tests; *p value <0.05; ***p value <0.001; ns, not significant).

(D) Proportion of γH2AX$^+$ cells after 24 h treatment with NCT02 as indicated and assessed by flow cytometry (two technical replicates per TSC; presented are mean ± SD; p values from unpaired, two-tailed t tests; *p value <0.05; **p value <0.01; ns, not significant).

(E) Ingenuity upstream regulator analysis of differentially expressed genes after treatment with NCT02. The top ten genes that regulate differentially expressed genes and might be modulated by treatment with NCT02 are presented and sorted according to p value (*Z* score >2 indicates activation; activation *Z* score <−2 indicates inhibition; NA, not applicable; inhibition is highlighted in blue).

See also Figure S1 and Table S4.

NCT02 triggers degradation of CCNK/CDK12 via the proteasome

CCNK and CDK12 were identified as top hits in both transcriptome- and proteome-based target deconvolution approaches. CDK13 was only found by mass spectrometry after affinity enrichment and was otherwise barely detectable in the TSCs by mass spectrometry or western blot. We thus focused on CCNK and CDK12 for further validation.

TPP pointed toward destabilization of CDK12 and decreased protein levels of CCNK after treatment with NCT02. Therefore, we tested increasing doses of NCT02 and assessed its impact on protein levels of CCNK and CDK12. Indeed, we observed a

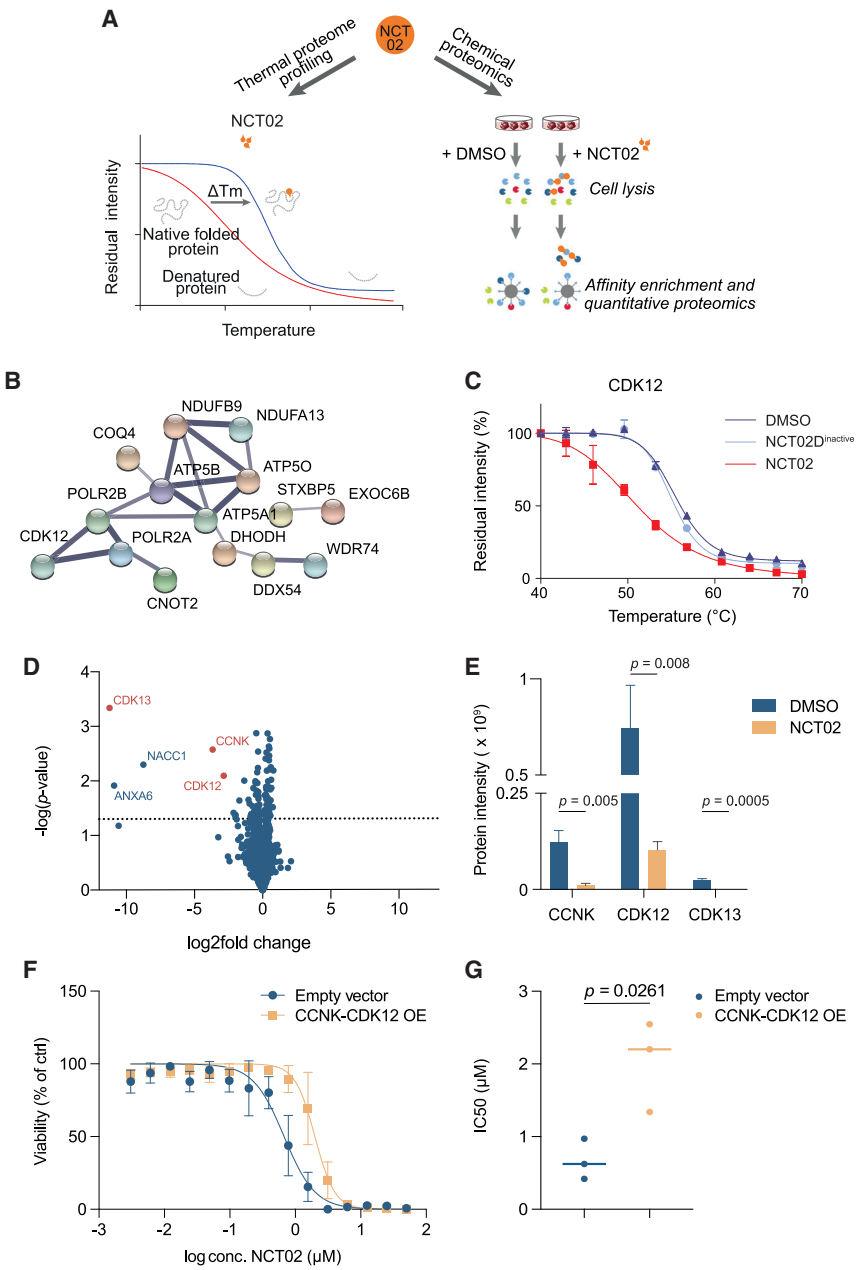

Figure 4. TPP and chemical proteomics identify CCNK/CDK12 as targets of NCT02

(A) Strategy for target deconvolution of NCT02.

(B) Proteins with significant thermal shift (ΔTm) after 2 h treatment of TSC03 cells with 10 μM NCT02. Presented are only those 15 proteins with a known protein-protein interaction with at least one additional of all proteins with a thermal shift as revealed by STRING protein-protein network analysis. Thickness of gray interaction lines indicates level of evidence for protein-protein interaction.

(C) Thermal shift analysis of CDK12 after treatment with NCT02, an inactive derivative of NCT02 (NCT02D^{inactive}) and DMSO (presented are mean ± SD).

(D) Quantitative mass spectrometry identifies proteins bound by an immobilized derivative of NCT02 (NCT02D^{active} with linker) after 2 h treatment of TSC03 cells with 10 μM unmodified NCT02 or DMSO before protein extraction (presented is the log_2fold change; dashed line indicates p value of 0.05; labeled are the top significantly depleted proteins and in red CCNK and its complex partners CDK12 and CDK13).

(E) Absolute protein levels (arbitrary units) of CCNK, CDK12, and CDK13 in pull-down with the immobilized NCT02D^{active} (same experiment as D) after treatment of cells with NCT02 or DMSO (p values from unpaired, two-tailed t tests; presented are mean + SD).

(F) Dose-response assays comparing sensitive TSC03 cells with empty vector or combined overexpression (OE) of CCNK and CDK12 treated with NCT02 (presented are mean ± SD and one representative of three biological replicates; conc., concentration).

(G) IC_{50} values of TSC03 cells with empty vector or combined overexpression of CCNK and CDK12 from the same experiment as (F). The bar represents the median from three biological replicates (p value from unpaired, two-tailed t test).

See also Figure S2 and Table S5.

concentration-dependent decrease of CCNK and CDK12 after NCT02 treatment in sensitive TSCs (Figure 5A), which was associated with a dose-dependent decrease of serine 2 phosphorylation of RNA polymerase 2 (POLR2), a known phosphorylation target site of CDK12. Levels of CDK9, which can also phosphorylate serine 2 of POLR2, and its target gene MCL1 were not affected by NCT02 (Figure 5A). Moreover, serine 5 phosphorylation of POLR2, which is the major target of CDK9, was not changed after NCT02 treatment (Figure S3A).

To examine kinetics of protein degradation, we assessed levels of CCNK (Figure 5B) and CDK12 (Figure 5C) at different time points after treatment. This analysis revealed that CCNK levels decreased less than 1 h after treatment with NCT02. Similarly, levels of CDK12 started declining 2 h after treatment in sensitive TSCs. Interestingly, decrease of CDK12 was also detected in two resistant TSCs after 2 h, but CDK12 protein levels increased back to baseline after 6 h, indicating that reduction of CDK12 protein levels was compensated in at least some resistant TSCs over time.

As transcript levels of CDK12 did not change significantly after treatment with NCT02 (Figure S2G), we tested whether active protein degradation was induced by NCT02. We treated sensitive TSC cells with either NCT02 alone or a combination of NCT02 and the proteasome inhibitor MG132. Indeed, protein levels of CCNK and CDK12, induction of apoptosis and the impact of NCT02 on cell viability could be partially rescued upon combination treatment (Figures 5D–5F), clearly indicating that the inhibitory effect of NCT02 was dependent on protein degradation.

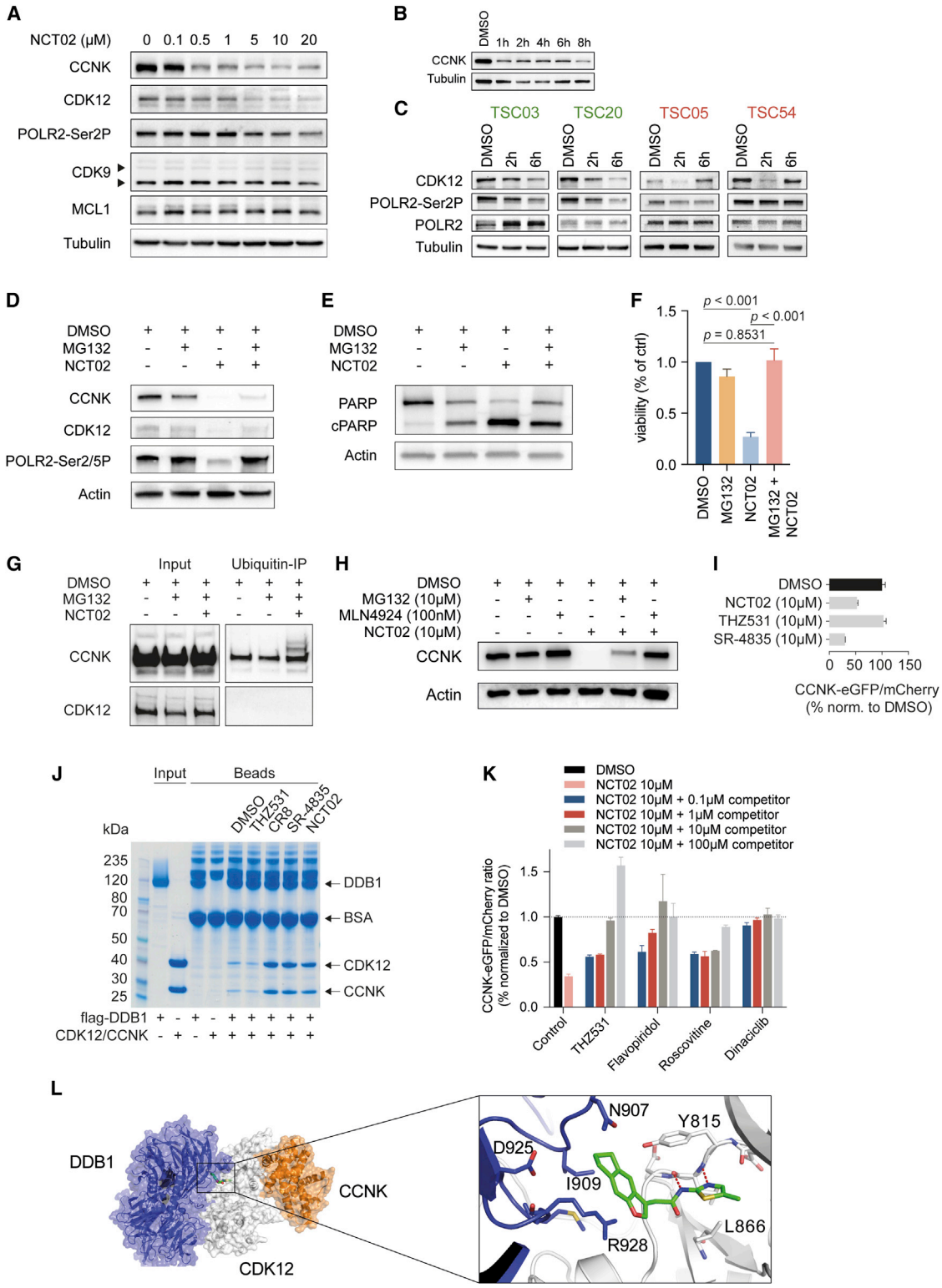

Figure 5. NCT02 triggers degradation of CCNK/CDK12

(A) Protein levels of CCNK, CDK12, and phosphorylation of POLR2 at serine 2 (POLR2-Ser2P) as well as CDK9 and its target MCL1 after 6 h treatment of TSC03 with NCT02 as indicated.

(B) Protein levels of CCNK at different time points of treatment of TSC03 with 10 μM NCT02.

(legend continued on next page)

NCT02 induces ubiquitination of CCNK via Cullin-RING ubiquitin ligases

To test whether degradation of CCNK and CDK12 was triggered by ubiquitination after compound treatment, ubiquitin coimmunoprecipitation (coIP) was performed. To prevent protein degradation, cells were treated with a combination of proteasome inhibitor and NCT02. After pull-down of ubiquitinated proteins, proteins were blotted and probed with antibodies against CCNK and CDK12, which revealed additional bands of higher molecular weight than the unmodified protein for CCNK, but not CDK12, after combination treatment (Figure 5G), indicating ubiquitination of CCNK induced by NCT02. In addition, basal levels of ubiquitinated CCNK were detectable after treatment with the proteasome inhibitor.

E3 ubiquitin ligases confer substrate specificity on the ubiquitin system, with Cullin-RING E3 ubiquitin ligases (CRE3s) being the largest family of E3 ubiquitin ligases whose activity is dependent on activation by the NEDD8-activating enzyme (NAE) (Bulatov and Ciulli, 2015). To test whether NCT02-induced CCNK-degradation was mediated by CRE3s, we performed a rescue experiment with the NAE inhibitor MLN4924. Combination treatment of TSC03 cells with NCT02 and MLN4924 revealed a substantial rescue of NCT02-induced CCNK degradation, demonstrating that NCT02-induced CCNK degradation is dependent on CRE3s (Figure 5H).

To assess whether induction of degradation of CCNK and CDK12 is a mechanism of action specific for NCT02 or generally triggered by other compounds binding to CDK12, a selective covalent CDK12/CDK13 inhibitor (THZ531) (Zhang et al., 2016) and a selective ATP-competitive CDK12/CDK13 inhibitor (SR-4835) (Quereda et al., 2019) were used, and protein levels of CCNK were determined using a CCNK-stability reporter in which CCNK is fused to eGFP (Słabicki et al., 2020). Despite high doses of THZ531, which were lethal for TSC cells over time, CCNK levels remained constant (Figures 5I and S3B). Surprisingly, treatment of TSC cells with SR-4835 induced degradation of CCNK (Figures 5I and S3B), comparable to NCT02, indicating that CCNK degradation can be triggered by structurally diverse compounds, and selective CDK12 inhibitors display a variable degree of kinase inhibition and degradation induction.

NCT02 acts as a molecular glue degrader of CCNK

Recently, molecular glue degraders that deplete CCNK were identified (Lv et al., 2020; Mayor-Ruiz et al., 2020; Słabicki et al., 2020). These compounds act by promoting an interaction between CCNK and the CUL4 adaptor protein DDB1 via CDK12, thereby presenting CCNK for ubiquitination and degradation. To test whether NCT02 acts as a molecular glue degrader of CCNK, we performed coIPs of recombinant FLAG-DDB1 in presence of the complex of recombinant CCNK and the kinase domain of CDK12, as well as different CDK12 inhibitors. These CDK12 inhibitors comprised the known molecular glue degrader CR8, the non-degrading CDK12 inhibitor THZ531, the CCNK-degrading CDK12 inhibitor SR-4835, and NCT02. Elution of the coIP proteins revealed high abundance of CCNK and CDK12 in the presence of CR8 and NCT02, whereas only very faint bands were visible after DMSO or THZ531 treatment (Figure 5J). This indicates that NCT02 mediates or significantly stabilizes an interaction between CDK12/CCNK and DDB1 comparable to the known molecular glue degrader CR8. This molecular glue activity was observed similarly for the selective CDK12/CDK13 inhibitor SR-4835.

To test whether NCT02-induced CCNK degradation was dependent on DDB1, we used single-guide RNAs (sgRNAs) targeting DDB1. As assessed by the CCNK-eGFP reporter, knockout of DDB1 resulted in decreased NCT02-induced CCNK degradation (Figures S3C and S3D). In addition, DDB1 knockout slightly reduced sensitivity to NCT02 in viability assays (Figure S3E).

Although binding or inhibition of CDK12 by NCT02 could not be detected in biochemical assays, we wondered whether NCT02 binds the kinase domain of CDK12 in living cells to act as a molecular glue between CDK12 and DDB1. Competition experiments in which NCT02-induced degradation of CCNK was quantified in the presence of increasing doses of compounds that bind the kinase domain of CDK12/CDK13 either covalently (THZ531) or reversibly (flavopiridol, roscovitine, or dinaciclib) (Figure 5K) revealed substantially decreased NCT02-induced CCNK degradation. Thus, CDK12/13 active site engagement is required for the degrader activity of NCT02.

Structure-based docking was used to explore the molecular interaction between NCT02 and CDK12. Within the CDK12/

(C) Protein levels of CDK12 and POLR2-Ser2P at different time points of treatment with 10 μM NCT02.
(D–F) Rescue of degradation of CCNK and CDK12 (D), cPARP levels (E), or cell viability (F) after 6 h co-treatment with 10 μM NCT02 and 10 μM MG132 (presented are mean + SD; p values from unpaired, two-tailed t tests; ctrl, control).
(G) Ubiquitin-immunoprecipitation (IP) and determination of CCNK and CDK12 levels in precipitated proteins after 6 h co-treatment with 10 μM NCT02 and 10 μM MG132.
(H) Rescue of NCT02-induced CCNK degradation by inhibition of proteasome (MG132) or Cullin-RING ubiquitin ligases (MLN4924; 6 h treatment for all compounds).
(I) CCNK degradation induced by 2 h treatment with indicated compounds and measured by flow cytometry using the CCNK-eGFP reporter (CCNK-eGFP level normalized to mCherry and DMSO; presented are mean + SD).
(J) CoIP of recombinant flag-DDB1 in the presence of untagged CCNK/CDK12 and individual compounds or DMSO.
(K) CCNK-eGFP degradation induced by 2 h treatment with NCT02 alone or in combination with increasing doses of competitive, non-degrading CDK12 inhibitors (presented are mean + SD).
(L) Left: *in silico*-modeling of binding pose of NCT02 with the CDK12/CCNK/DDB1 ternary complex. Right: details of NCT02 binding pose (O, N, and S atoms in red, blue, and yellow, respectively; C atoms are colored according to parent protein; red dotted lines indicate specific hydrogen-bonding interactions between NCT02 and CDK12).
See also Figure S3.

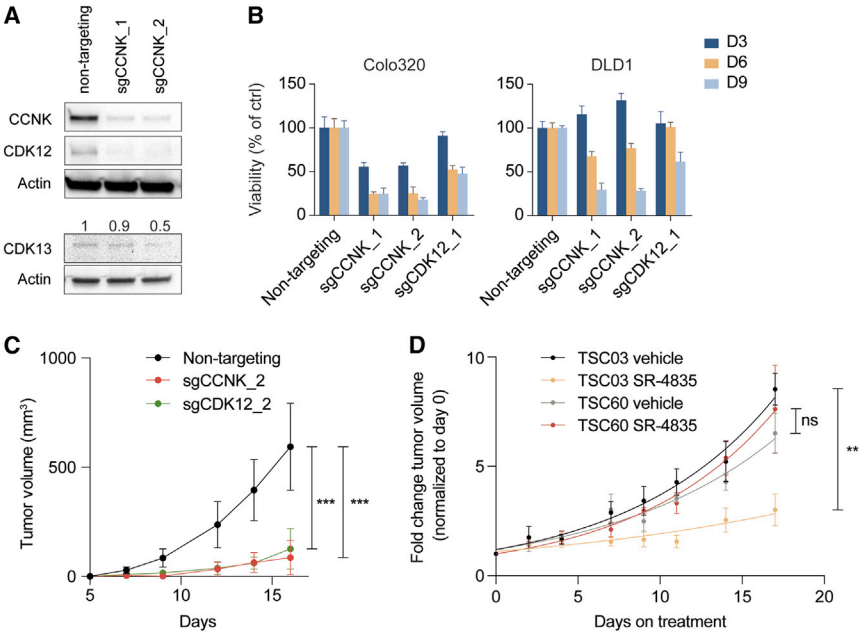

Figure 6. Knockout of CCNK and CDK12 decreases viability of CRC cell lines

(A) Protein levels of CCNK, CDK12, and CDK13 after CRISPR/Cas9-based knockout of CCNK in Colo320 cells.

(B) Time course assessment of viability in Colo320 and DLD1 cells after CRISPR/Cas9-based knockout of CCNK or CDK12 three (D3), six (D6), and nine (D9) days after infection, normalized to non-targeting control (ctrl, control; presented are mean + SD).

(C) DLD1 knockout cell lines were injected in NSG mice and tumor growth was monitored over time (n = 4 mice per group; presented are mean ± SEM; *** corresponds to a p value <0.001 as calculated by unpaired, two-tailed t tests).

(D) TSC03 and TSC60 cells were injected in NSG mice. After tumor formation mice were treated with SR-4835 (20 mg/kg orally 5 days/week) and tumor growth rate was analyzed (n = 6 mice per group; presented are mean ± SEM; **corresponds to a p value <0.01 as calculated by unpaired, two-tailed t tests; ns, not significant; curves represent fit exponential growth curves).

See also Figure S4.

CCNK/DDB1 structure (Słabicki et al., 2020), the NCT02 aminothiazole binds at the ATP binding site where it forms two specific hydrogen bonds to methionine 816 backbone atoms (Figure 5L). Via the methyl linker, the dihydro-indenofuran moiety extends out of the kinase active site and occupies a pocket in the adjacent DDB1 protein. The inactive compound NCT02D^{inactive}, with a longer ethyl linker, cannot be accommodated in a similar binding mode due to severe steric hinderance with the DDB1 protein. Interestingly, superposition of the NCT02 docking with the X-ray of CDK12/CCNK/DDB1 in complex with molecular glue CR8 predicts strong similarity between the binding modes of the two compounds (Figure S3F).

In summary, these experiments strongly indicate that NCT02 acts as a molecular glue by mediating an interaction between CCNK and DDB1 in living cells presumably via CDK12.

Knockout of CDK12 and CCNK decreases tumor growth

To test whether loss of CCNK is sufficient to decrease CDK12 levels and assess the effect of CCNK and CDK12 knockout on viability of CRC cells, CRISPR/Cas9-based knockout cell lines (DLD1 and Colo320) were generated.

Notably, loss of CCNK resulted in a decrease of CDK12 and CDK13 levels (Figures 6A and S4A), confirming the relevance of complex formation for the stability of these binding partners. In addition, CCNK knockout resulted in a pronounced decrease of viability in both cell lines (Figure 6B). Similarly, viability was reduced after knockout of CDK12 *in vitro* (Figure 6B). Moreover, tumor growth was significantly diminished after xenotransplantation of DLD1 cells with CDK12- or CCNK-knockout compared to controls *in vivo* (Figure 6C). Thus, loss of CCNK and CDK12 decreased viability of CRC cells, suggesting that degradation of these proteins by NCT02 at least contributed to its inhibitory effect.

Targeted CCNK/CDK12 degradation shows anti-tumor activity in CRC PDXs

To test whether TSC-derived PDXs show differential sensitivity to targeted degradation of CCNK/CDK12 *in vivo*, we transplanted TSC03 cells that were sensitive to NCT02 and TSC60 cells that were resistant to NCT02 *in vitro* into immunodeficient mice. Because NCT02 was metabolically not stable enough for *in vivo* experiments, we treated PDXs with SR-4835 that highly selectively binds CDK12 and CDK13, induces degradation of CCNK similar to NCT02, and shows a differential sensitivity pattern across different TSCs comparable to NCT02 (Figure S4B). SR-4835 halted tumor growth in PDXs derived from TSC03, whereas PDXs derived from TSC60 cells continued growing despite treatment (Figure 6D), indicating that the heterogeneous response profile of TSCs from our biobank toward targeted CDK12/CCNK degradation was recapitulated *in vivo* and confirming its therapeutic value for a subset of CRC.

TP53-deficient TSCs assigned to CMS4 are particularly sensitive to NCT02

To identify potential molecular markers associated with response to NCT02, we correlated sensitivity of individual TSCs to NCT02 with transcriptomic and genomic data including mutational signatures (Figures 1B and 7A).

Because alterations of CDK12 and CCNK may affect the response to targeted CCNK/CDK12 degradation, we searched for CDK12/CCNK alterations in TSCs. Copy number alterations involving CDK12 or CCNK were detected but distributed similarly across sensitive and resistant TSCs (Figure S4C). Two CDK12 mutations were found in sensitive TSCs, one of them being a nonsense mutation, the other one being a missense mutation of unknown significance outside the kinase domain. One

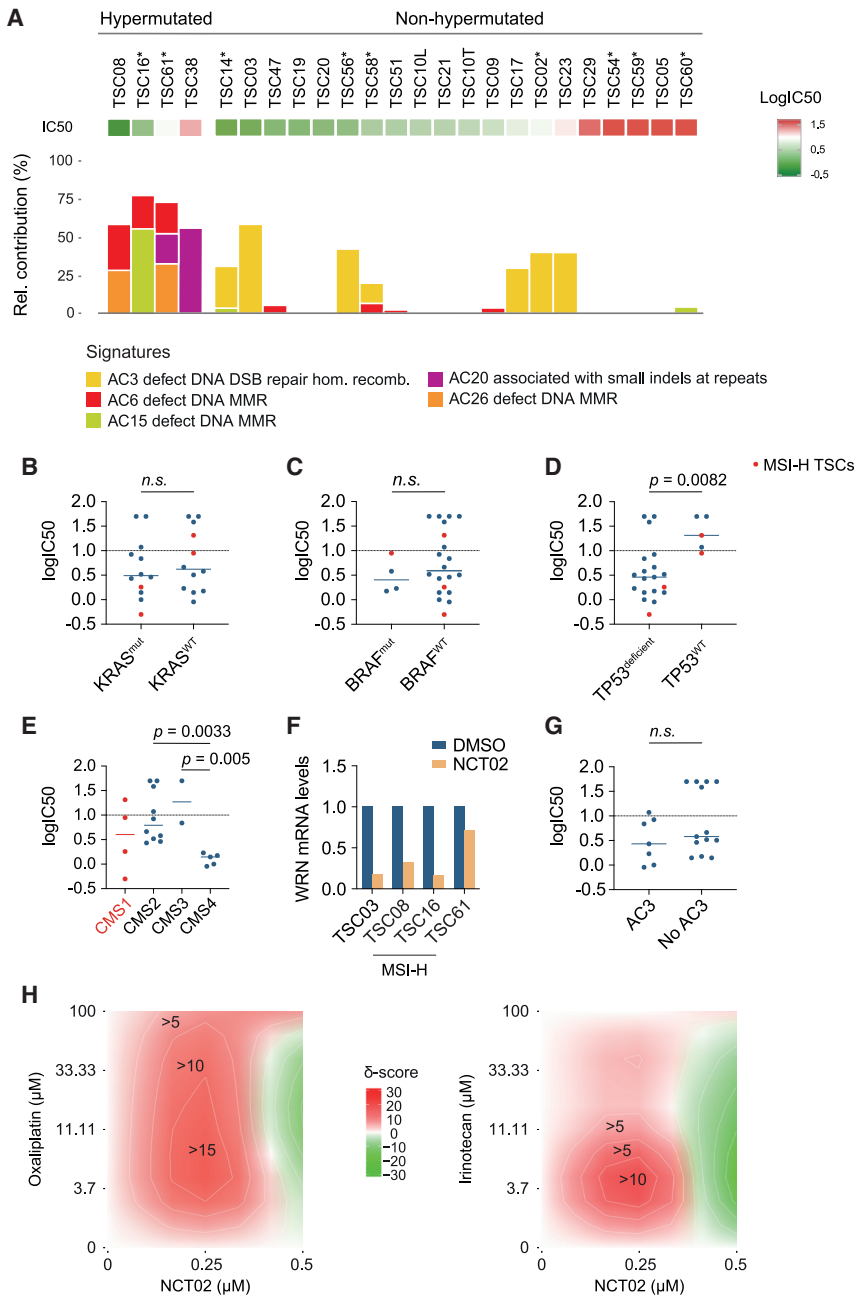

Figure 7. TP53-deficient TSCs assigned to CMS4 are particularly sensitive to NCT02

(A) Relative contribution of individual mutational signatures related to DNA damage repair defects (Alexandrov et al., 2013) to overall mutations detected by whole-exome or whole-genome sequencing (the latter marked by asterisks; AC, Alexandrov cosmic; DSB, double-strand break; MMR, mismatch repair; indel, insertion or deletion; rel, relative).

(B–E and G) Association of selected mutations, CMS, and mutational signature AC3 with sensitivity toward NCT02 (lines indicate mean; p values from unpaired, two-tailed t tests; ns, not significant).

(F) mRNA levels of *WRN* after 24 h treatment with 5 μM NCT02 (normalized to actin and DMSO).

(H) Bliss synergy plots from dilutions of oxaliplatin or irinotecan in combination with fixed doses of NCT02 on TSC03 cells (δ-score <−10 indicates likely antagonistic effect, δ >−10 and <10 indicates likely additive effect, and δ >10 likely indicates synergistic effect).

See also Figure S4.

missense mutation within the kinase domain of CDK12 (I792N) was found in the resistant TSC38, potentially affecting the interaction of CDK12 with CCNK, which occurs via the kinase domain (Lv et al., 2020). In addition, one nonsense mutation of CCNK was found in a sensitive hypermutated TSC.

Next, we were interested in two subgroups of CRCs that are characterized by activating mutations in KRAS ($KRAS^{mut}$) or BRAF ($BRAF^{mut}$) and associated with poor prognosis. We found that wild-type KRAS and $KRAS^{mut}$ TSCs were similarly sensitive (Figure 7B). Moreover, four TSCs with activating BRAF mutations showed comparable sensitivity to NCT02 as wild-type BRAF TSCs (Figure 7C). Thus, NCT02 might be a treatment option for both unfavorable CRC subgroups.

Interestingly, TSCs with inactivating mutations or loss of TP53 did show a significantly higher sensitivity to NCT02 (Figure 7D). Whereas TSCs with wild-type TP53 were rather homogenously resistant, most $TP53^{deficient}$ TSCs were sensitive. Still, three out of 21 $TP53^{deficient}$ TSCs also appeared resistant, indicating that TP53 deficiency might be important, but not sufficient to induce sensitivity.

Based on transcriptomic profiles, TSCs were assigned to different CMSs. CMS1 marks highly microsatellite-instable (MSI-H) and hypermutated TSCs (Guinney et al., 2015). Three out of four CMS1 TSCs were sensitive to NCT02 (Figure 7E). Interestingly, recent reports have identified *WRN* as a synthetically lethal target of MSI-H cancers, and *WRN* has been proposed to be a CDK12 target (Chan et al., 2019; Dubbury et al., 2018). Indeed, *WRN* mRNA levels were downregulated after treatment with NCT02 (Figure 7F), potentially explaining the sensitivity of MSI-H TSCs to NCT02.

In microsatellite-stable (MSS) CRCs, CMS2 and CMS3 identify epithelial CRCs, and CMS4 defines a mesenchymal CRC subtype associated with unfavorable prognosis. Notably, TSCs belonging to CMS4 were significantly more sensitive than TSCs assigned to CMS2 or CMS3 (Figure 7E). Thus, CMS4 might represent a subset of MSS CRCs particularly sensitive to NCT02.

It has been suggested that DNA damage response (DDR) deficiencies may sensitize to ATM/ATR inhibitors due to increased reliance on DDR checkpoints (Weber and Ryan, 2015). Because NCT02 induced transcriptional downregulation of ATM and ATR (Figure 3C), we wondered whether TSCs with DDR deficiencies were sensitive to NCT02. The mutational signature AC3 identifies MSS cancers with homologous recombination repair deficiency (Alexandrov et al., 2020). Interestingly, we detected eight MSS TSCs with AC3 contribution to the mutational catalog that were rather sensitive to NCT02 (Figure 7G).

To assess whether TP53 status and CMS of CRC cell lines indicated dependency on transcriptional programs regulated by CCNK/CDK12 or CCNK/CDK13, we analyzed "Fitness Scores" that were calculated from large-scale genome-wide CRISPR/Cas9 screens across 31 independent CRC cell lines and represent a quantitative measure of the reduction of cell viability elicited by a gene inactivation via CRISPR/Cas9 (https://score.depmap.sanger.ac.uk) (Behan et al., 2019; van der Meer et al., 2019). Knockout of CDK12 had a significant impact on viability in a subset of all CRC cell lines (nine out of 31), whereas knockout of CDK13 did not show a significant reduction of viability in any of these cell lines (Figure S4). There was a trend for higher Fitness Scores for CDK12 (lower impact of gene knockout on viability) in $TP53^{wild\text{-}type}$ cell lines compared to $TP53^{deficient}$ cell lines and a trend toward lower scores (higher impact of gene knockout on viability) in CMS1 and CMS4 compared to CMS2/3 cell lines. When we combined CMS and TP53 deficiency, CMS4 $TP53^{deficient}$ cell lines showed significantly lower scores compared to the remaining $TP53^{deficient}$ MSS CRC cell lines (Figure S4), similar to the particular sensitivity of CMS4 TSCs (that were all $TP53^{deficient}$) to NCT02.

NCT02 sensitizes TSC cells for standard chemotherapy

Synergy between CDK12 kinase inhibitors and drugs causing DNA damage or interfering with DNA damage repair pathways has recently been reported in other tumor entities (Quereda et al., 2019). We thus tested combinations of fixed NCT02 concentrations with serial dilutions of oxaliplatin or irinotecan, which are both routinely used for treatment of metastatic CRC. The Bliss reference model was applied to calculate synergy scores (Ianevski et al., 2019) and identified dose combinations of NCT02 and oxaliplatin or irinotecan, respectively, that were highly likely to be synergistic (Figure 7H).

DISCUSSION

Here, we identified NCT02 in a high-throughput compound screen on patient-derived CRC spheroids. Transcriptomic and proteomic approaches characterized NCT02 as a molecular glue degrader that depletes CCNK and induces degradation of its binding partners CDK12 and CDK13. In contrast to CDK13, knockout of CDK12 significantly decreased viability in a subset of CRC cell lines, suggesting that the inhibitory effect of NCT02 was rather depending on CCNK/CDK12 than CCNK/CDK13 function. CDK12 forms a complex with CCNK to act as a transcriptional regulator of genes critically involved in DDR pathways (Blazek et al., 2011; Krajewska et al., 2019). Accordingly, multiple genes of the DDR pathways were transcriptionally suppressed, and increased DNA damage was detected after treatment with NCT02.

Chemical proteomics with living cells indicated binding of NCT02 to CCNK, CDK12, and CDK13. However, biochemical TPP and conventional competitive pull-down assays, in which cell extracts instead of living cells were incubated with NCT02, did not identify any direct binding partner, consistent with the observation that molecular glues frequently bind to their target proteins with low or undetectable affinities (Lv et al., 2020).

Recently, additional, but structurally different, molecular glue degraders of CCNK/CDK12 have been reported (Lv et al., 2020; Mayor-Ruiz et al., 2020; Słabicki et al., 2020). These molecules induce complex formation between CDK12/CCNK and the CUL4 adaptor protein DDB1, presenting CCNK for ubiquitination and degradation via DDB1-CUL4-RBX1 ubiquitin ligases. Accordingly, coIP experiments revealed molecular glue activity of NCT02 by binding to CCNK/CDK12 and DDB1. *In silico*-modeling revealed a surface-exposed moiety of NCT02 likely to mediate the interaction between the CCNK/CDK12 complex and DDB1, which further supports the hypothesis that surface-exposed moieties can confer gain-of-function glue properties to compounds (Słabicki et al., 2020). Knockout of DDB1 decreased NCT02-induced CCNK degradation, indicating a functional role of DDB1-CUL4-RBX1 ubiquitin ligases in mediating NCT02-induced CCNK degradation.

Notably, the lack of detectable CDK12 kinase inhibitory activity distinguishes NCT02 from CR8 and SR-4835 that both act as degrader and kinase inhibitors. Given the availability of selective CDK12 kinase inhibitors without degrader activity (e.g., THZ531) (Zhang et al., 2016), future studies might assess how chemical modifications impact on degrader versus kinase inhibitory activity of compounds and how their balance effects on- and off-target toxicity.

The comprehensive molecular analysis of our biobank allowed for testing associations of drug responses and genomic features, although the limited size of 24 TSCs was not expected to provide robust statistics. Still, TSCs with inactivating TP53 mutations were found to be significantly more sensitive to NCT02 than those with wild-type TP53. Interestingly, an association of TP53-deficiency and sensitivity to ATR inhibitors has been described as profound synthetic lethality (Reaper et al., 2011; Toledo et al., 2011), and NCT02 treatment suppressed expression of the CDK12 target gene ATR.

In addition, all TSCs assigned to CMS4 were significantly more sensitive than other MSS CMSs. CMS4 is associated with particularly poor prognosis (Guinney et al., 2015) and a TIC-like and/or epithelial-mesenchymal transition (EMT) signature (Le Corre et al., 2019), further suggesting that our screen layout using TIC-enriched TSCs identified a compound with activity against TIC-rich tumors. An independent dataset from large-scale genome-wide CRISPR/Cas9 screens across CRC cell lines revealed a similar pattern of particular dependency on CDK12 in CMS4 and $TP53^{deficient}$ CRC cell lines, providing further evidence for a particular vulnerability of this subset of patients with CRC for loss of CDK12.

A limitation of our study is that the heterogeneous nature of our biobank of CRC TSCs with differences in e.g., tolerance of

dissociation methods and cell sorting, efficiency of the CRISPR/Cas9 system, and resistance toward selection antibiotics, required selection of individual TSCs suitable for individual secondary assays. Moreover, NCT02 could not be applied in animal experiments and its potency thus not be tested *in vivo*. However, identification of molecular glue and CCNK degrader activity of SR-4835 allowed for testing targeted CCNK/CDK12 degradation as a therapeutic approach in PDXs.

Although SR-4835 halted tumor growth of CMS4 PDX, combination therapies might be necessary to induce tumor regression. We thus investigated and showed that targeted CCNK/CDK12 degradation synergizes *in vitro* with oxaliplatin and irinotecan that are both part of chemotherapy regimen for metastatic CRC (Grothey et al., 2004). Because we did not test these combinations *in vivo*, we cannot formally rule out that these combination therapies might act less synergistically *in vivo*.

Although CDK12 has only recently emerged as a potential vulnerability for different cancer types including Ewing sarcoma, triple-negative breast cancer, and hepatocellular carcinoma (Iniguez et al., 2018; Quereda et al., 2019; Wang et al., 2020), we describe here a profound CDK12 dependency in a subgroup of patients with CRC. Beyond identification of a promising target for a subgroup of CRCs, our findings show that our strategy of hit selection from a phenotypic screen can identify selective compounds and relevant cancer targets.

In summary, NCT02 adds a different small molecule to the spectrum of drug-induced proteolysis, which has just recently begun to be exploited by the class of proteolysis targeting chimeras (PROTACs) and molecular glue degraders and might open new therapeutic strategies for many tumor types including CRC by expanding the druggable proteome.

STAR★METHODS

Detailed methods are provided in the online version of this paper and include the following:

- KEY RESOURCES TABLE
- RESOURCE AVAILABILITY
  - Lead contact
  - Materials availability
  - Data and code availability
- EXPERIMENTAL MODEL AND SUBJECT DETAILS
  - Primary CRC TSCs
  - CRC cell lines
  - Mice models
- METHOD DETAILS
  - DNA- and RNA-sequencing of TSCs
  - High-throughput compound screen on TSC cells
  - Individual drug assays
  - Drug competition assays
  - Synergy assessment
  - *In vitro* biochemical profiling of NCT02
  - Analysis of differentially expressed genes
  - Ingenuity® pathway and upstream regulator analysis
  - qRT-PCR
  - γH2AX staining
  - Spheroid formation assays
  - Analysis of cell cycle and apoptosis
  - Thermal proteome profiling
  - Chemical proteomics
  - LC-MS/MS analysis
  - Synthesis of derivatives
  - Rescue experiments using CCNK/CDK12-overexpression
  - Western blots
  - Rescue experiments using inhibitors of proteasome or ubiquitin ligases
  - Ubiquitin immunoprecipitation
  - Quantification of CCNK degradation using the CCNK-eGFP reporter
  - Co-immunoprecipitation of CCNK/CDK12 with FLAG-DDB1
  - *In silico*-modeling of NCT02 binding mode
  - CRISPR/Cas9 editing
  - Tumor formation
  - Fitness scores and sequencing data from CRC cell line panel
- QUANTIFICATION AND STATISTICAL ANALYSIS

SUPPLEMENTAL INFORMATION

Supplemental information can be found online at https://doi.org/10.1016/j.celrep.2021.109394.

ACKNOWLEDGMENTS

We thank Martin Schneider (Department of General, Visceral and Transplantation Surgery, Heidelberg University Hospital, Heidelberg, Germany) for providing clinical samples and Tim Kindinger, Hannah Walzer, and Ina Siebig (NCT and DKFZ Heidelberg) as well as Elzbieta Wiecko and Sabine Schnabel (Nuvisan ICB GmbH) for excellent technical support. We acknowledge support of the Chemical Biology Core Facility of EMBL, DKFZ and University of Heidelberg, as well as the Flow Cytometry Core Facility of the DKFZ. We thank the DKFZ Sample Processing Laboratory for sample preparation and the Microarray and High Throughput Sequencing Units of the DKFZ Genomics and Proteomics Core Facility for sequencing. We thank Sandra Poser and Svenja Wiechmann (OmicScouts GmbH) for technical assistance and Thomas Wieland (OmicScouts GmbH, currently: FMI Germany GmbH) for bioinformatics support. The project was jointly funded and supported by DKFZ and Bayer in the frame of their strategic alliance. Moreover, this work was supported by grants from the NCT 3.0 Precision Oncology Program (NCT3.0_2015.4 TransOnco and NCT3.0_2015.54 DysregPT) to H.G., the EU Framework Program Horizon 2020 (TRANSCAN-2 ERANET, TACTIC consortium to H.G.), and the Deutsche Krebshilfe Priority program "Translational Oncology" (Colon-Resist-Net to H.G. and C.R.B.). DKFZ-HIPO provided technical support and funding (HIPO-H012 and HIPO-K01A). S.M.D. was supported by a scholarship from the Heidelberg School of Oncology. P.L.C. was supported by a DKFZ postdoctoral fellowship. K.L. was supported by a scholarship from the DKFZ graduate school.

AUTHOR CONTRIBUTIONS

Conceptualization, S.M.D., S.J., M.L., and H.G.; investigation, S.M.D., C.S., P.L.C., M.H., A.L.O.-P., E.S., M.K.Z., S.M., K.L., M.B., S.K., F.W., A.B., U.U., K.P., J.L., A.H., D.M., S.J.H., U.S., J.W., L.-M.T., G. Siemeister, C.R.B., B.K., G. Stoehr, H.H., S.J., and M.L.; writing – original draft, S.M.D. and H.G.; writing – review & editing, S.M.D., P.L.C., M.H., C.R.B., H.H., F.H., and H.G.; funding acquisition, S.M.D., S.K., F.W., D.M., G. Siemeister, S.J., M.L., F.H., and H.G.; resources, A.N.; supervision, S.M.D., F.H., and H.G.

DECLARATION OF INTERESTS

C.S. is an employee of Merck KGaA. P.L.C. is an employee of CureVac AG. A.N. is an employee of Spark Therapeutics Inc. A.H., D.M., S.J.H., U.S., J.W., L.-M.T., G.S., S.J., and M.L. are or were employees of Bayer AG and are shareholders or may have additional stock options. U.S., J.W., L.M.T., G. Stoehr, S.J.H., G. Siemeister, and M.L. are employees of Nuvisan ICB GmbH. G. Stoehr and H.H. are employees of OmicScouts GmbH. B.K. and H.H. are shareholders of OmicScouts GmbH. All other authors declare no competing interests.

Received: September 23, 2020
Revised: April 8, 2021
Accepted: June 23, 2021
Published: July 20, 2021

REFERENCES

Alexandrov, L.B., Nik-Zainal, S., Wedge, D.C., Aparicio, S.A., Behjati, S., Biankin, A.V., Bignell, G.R., Bolli, N., Borg, A., Børresen-Dale, A.L., et al.; Australian Pancreatic Cancer Genome Initiative; ICGC Breast Cancer Consortium; ICGC MMML-Seq Consortium; ICGC PedBrain (2013). Signatures of mutational processes in human cancer. Nature *500*, 415–421.

Alexandrov, L.B., Kim, J., Haradhvala, N.J., Huang, M.N., Tian Ng, A.W., Wu, Y., Boot, A., Covington, K.R., Gordenin, D.A., Bergstrom, E.N., et al.; PCAWG Mutational Signatures Working Group; PCAWG Consortium (2020). The repertoire of mutational signatures in human cancer. Nature *578*, 94–101.

Barette, C., Jariel-Encontre, I., Piechaczyk, M., and Piette, J. (2001). Human cyclin C protein is stabilized by its associated kinase cdk8, independently of its catalytic activity. Oncogene *20*, 551–562.

Behan, F.M., Iorio, F., Picco, G., Gonçalves, E., Beaver, C.M., Migliardi, G., Santos, R., Rao, Y., Sassi, F., Pinnelli, M., et al. (2019). Prioritization of cancer therapeutic targets using CRISPR-Cas9 screens. Nature *568*, 511–516.

Blazek, D., Kohoutek, J., Bartholomeeusen, K., Johansen, E., Hulinkova, P., Luo, Z., Cimermancic, P., Ule, J., and Peterlin, B.M. (2011). The Cyclin K/Cdk12 complex maintains genomic stability via regulation of expression of DNA damage response genes. Genes Dev. *25*, 2158–2172.

Bormann, F., Rodríguez-Paredes, M., Lasitschka, F., Edelmann, D., Musch, T., Benner, A., Bergman, Y., Dieter, S.M., Ball, C.R., Glimm, H., et al. (2018). Cell-of-Origin DNA Methylation Signatures Are Maintained during Colorectal Carcinogenesis. Cell Rep. *23*, 3407–3418.

Bulatov, E., and Ciulli, A. (2015). Targeting Cullin-RING E3 ubiquitin ligases for drug discovery: structure, assembly and small-molecule modulation. Biochem. J. *467*, 365–386.

Cancer Genome Atlas, N.; Cancer Genome Atlas Network (2012). Comprehensive molecular characterization of human colon and rectal cancer. Nature *487*, 330–337.

Chan, E.M., Shibue, T., McFarland, J.M., Gaeta, B., Ghandi, M., Dumont, N., Gonzalez, A., McPartlan, J.S., Li, T., Zhang, Y., et al. (2019). WRN helicase is a synthetic lethal target in microsatellite unstable cancers. Nature *568*, 551–556.

Cox, J., Hein, M.Y., Luber, C.A., Paron, I., Nagaraj, N., and Mann, M. (2014). Accurate proteome-wide label-free quantification by delayed normalization and maximal peptide ratio extraction, termed MaxLFQ. Mol. Cell. Proteomics *13*, 2513–2526.

Dagogo-Jack, I., and Shaw, A.T. (2018). Tumour heterogeneity and resistance to cancer therapies. Nat. Rev. Clin. Oncol. *15*, 81–94.

Dieter, S.M., Ball, C.R., Hoffmann, C.M., Nowrouzi, A., Herbst, F., Zavidij, O., Abel, U., Arens, A., Weichert, W., Brand, K., et al. (2011). Distinct types of tumor-initiating cells form human colon cancer tumors and metastases. Cell Stem Cell *9*, 357–365.

Dieter, S.M., Giessler, K.M., Kriegsmann, M., Dubash, T.D., Möhrmann, L., Schulz, E.R., Siegl, C., Weber, S., Strakerjahn, H., Oberlack, A., et al. (2017a). Patient-derived xenografts of gastrointestinal cancers are susceptible to rapid and delayed B-lymphoproliferation. Int. J. Cancer *140*, 1356–1363.

Dieter, S.M., Heining, C., Agaimy, A., Huebschmann, D., Bonekamp, D., Hutter, B., Ehrenberg, K.R., Fröhlich, M., Schlesner, M., Scholl, C., et al. (2017b). Mutant KIT as imatinib-sensitive target in metastatic sinonasal carcinoma. Ann. Oncol. *28*, 142–148.

Dubbury, S.J., Boutz, P.L., and Sharp, P.A. (2018). CDK12 regulates DNA repair genes by suppressing intronic polyadenylation. Nature *564*, 141–145.

Eder, J., Sedrani, R., and Wiesmann, C. (2014). The discovery of first-in-class drugs: origins and evolution. Nat. Rev. Drug Discov. *13*, 577–587.

Eide, P.W., Bruun, J., Lothe, R.A., and Sveen, A. (2017). CMScaller: an R package for consensus molecular subtyping of colorectal cancer pre-clinical models. Sci. Rep. *7*, 16618.

Follenzi, A., Ailles, L.E., Bakovic, S., Geuna, M., and Naldini, L. (2000). Gene transfer by lentiviral vectors is limited by nuclear translocation and rescued by HIV-1 pol sequences. Nat. Genet. *25*, 217–222.

Franken, H., Mathieson, T., Childs, D., Sweetman, G.M., Werner, T., Tögel, I., Doce, C., Gade, S., Bantscheff, M., Drewes, G., et al. (2015). Thermal proteome profiling for unbiased identification of direct and indirect drug targets using multiplexed quantitative mass spectrometry. Nat. Protoc. *10*, 1567–1593.

Giessler, K.M., Kleinheinz, K., Huebschmann, D., Balasubramanian, G.P., Dubash, T.D., Dieter, S.M., Siegl, C., Herbst, F., Weber, S., Hoffmann, C.M., et al. (2017). Genetic subclone architecture of tumor clone-initiating cells in colorectal cancer. J. Exp. Med. *214*, 2073–2088.

Grothey, A., Sargent, D., Goldberg, R.M., and Schmoll, H.J. (2004). Survival of patients with advanced colorectal cancer improves with the availability of fluorouracil-leucovorin, irinotecan, and oxaliplatin in the course of treatment. J. Clin. Oncol. *22*, 1209–1214.

Guinney, J., Dienstmann, R., Wang, X., de Reyniès, A., Schlicker, A., Soneson, C., Marisa, L., Roepman, P., Nyamundanda, G., Angelino, P., et al. (2015). The consensus molecular subtypes of colorectal cancer. Nat. Med. *21*, 1350–1356.

Hahne, H., Pachl, F., Ruprecht, B., Maier, S.K., Klaeger, S., Helm, D., Médard, G., Wilm, M., Lemeer, S., and Kuster, B. (2013). DMSO enhances electrospray response, boosting sensitivity of proteomic experiments. Nat. Methods *10*, 989–991.

Horak, P., Uhrig, S., Witzel, M., Gil-Farina, I., Hutter, B., Rath, T., Gieldon, L., Balasubramanian, G.P., Pastor, X., Heilig, C.E., et al. (2020). Comprehensive genomic characterization of gene therapy-induced T-cell acute lymphoblastic leukemia. Leukemia *34*, 2785–2789.

Ianevski, A., Giri, A.K., Gautam, P., Kononov, A., Potdar, S., Saarela, J., Wennerberg, K., and Aittokallio, T. (2019). Prediction of drug combination effects with a minimal set of experiments. Nat. Mach. Intell. *1*, 568–577.

Iniguez, A.B., Stolte, B., Wang, E.J., Conway, A.S., Alexe, G., Dharia, N.V., Kwiatkowski, N., Zhang, T., Abraham, B.J., Mora, J., et al. (2018). EWS/FLI Confers Tumor Cell Synthetic Lethality to CDK12 Inhibition in Ewing Sarcoma. Cancer Cell *33*, 202–216.e6.

Ishiguro, T., Ohata, H., Sato, A., Yamawaki, K., Enomoto, T., and Okamoto, K. (2017). Tumor-derived spheroids: Relevance to cancer stem cells and clinical applications. Cancer Sci. *108*, 283–289.

Jafari, R., Almqvist, H., Axelsson, H., Ignatushchenko, M., Lundbäck, T., Nordlund, P., and Martinez Molina, D. (2014). The cellular thermal shift assay for evaluating drug target interactions in cells. Nat. Protoc. *9*, 2100–2122.

Krajewska, M., Dries, R., Grassetti, A.V., Dust, S., Gao, Y., Huang, H., Sharma, B., Day, D.S., Kwiatkowski, N., Pomaville, M., et al. (2019). CDK12 loss in cancer cells affects DNA damage response genes through premature cleavage and polyadenylation. Nat. Commun. *10*, 1757.

Krönke, J., Udeshi, N.D., Narla, A., Grauman, P., Hurst, S.N., McConkey, M., Svinkina, T., Heckl, D., Comer, E., Li, X., et al. (2014). Lenalidomide causes selective degradation of IKZF1 and IKZF3 in multiple myeloma cells. Science *343*, 301–305.

Le Corre, D., Ghazi, A., Balogoun, R., Pilati, C., Aparicio, T., Martin-Lannerée, S., Marisa, L., Djouadi, F., Poindessous, V., Crozet, C., et al. (2019). The

cellular prion protein controls the mesenchymal-like molecular subtype and predicts disease outcome in colorectal cancer. EBioMedicine *46*, 94–104.

Li, L., Ugalde, A.P., Scheele, C.L.G.J., Dieter, S.M., Nagel, R., Ma, J., Pataskar, A., Korkmaz, G., Elkon, R., Chien, M.P., et al. (2021). A comprehensive enhancer screen identifies TRAM2 as a key and novel mediator of YAP oncogenesis. Genome Biol. *22*, 54.

Linnekamp, J.F., Hooff, S.R.V., Prasetyanti, P.R., Kandimalla, R., Buikhuisen, J.Y., Fessler, E., Ramesh, P., Lee, K.A.S.T., Bochove, G.G.W., de Jong, J.H., et al. (2018). Consensus molecular subtypes of colorectal cancer are recapitulated in in vitro and in vivo models. Cell Death Differ. *25*, 616–633.

Lv, L., Chen, P., Cao, L., Li, Y., Zeng, Z., Cui, Y., Wu, Q., Li, J., Wang, J.H., Dong, M.Q., et al. (2020). Discovery of a molecular glue promoting CDK12-DDB1 interaction to trigger cyclin K degradation. eLife *9*, e59994.

Ma, X., Liu, Y., Liu, Y., Alexandrov, L.B., Edmonson, M.N., Gawad, C., Zhou, X., Li, Y., Rusch, M.C., Easton, J., et al. (2018). Pan-cancer genome and transcriptome analyses of 1,699 paediatric leukaemias and solid tumours. Nature *555*, 371–376.

Martinez Molina, D., Jafari, R., Ignatushchenko, M., Seki, T., Larsson, E.A., Dan, C., Sreekumar, L., Cao, Y., and Nordlund, P. (2013). Monitoring drug target engagement in cells and tissues using the cellular thermal shift assay. Science *341*, 84–87.

Mayor-Ruiz, C., Bauer, S., Brand, M., Kozicka, Z., Siklos, M., Imrichova, H., Kaltheuner, I.H., Hahn, E., Seiler, K., Koren, A., et al. (2020). Rational discovery of molecular glue degraders via scalable chemical profiling. Nat. Chem. Biol. *16*, 1199–1207.

Médard, G., Pachl, F., Ruprecht, B., Klaeger, S., Heinzlmeir, S., Helm, D., Qiao, H., Ku, X., Wilhelm, M., Kuehne, T., et al. (2015). Optimized chemical proteomics assay for kinase inhibitor profiling. J. Proteome Res. *14*, 1574–1586.

Moffat, J.G., Rudolph, J., and Bailey, D. (2014). Phenotypic screening in cancer drug discovery - past, present and future. Nat. Rev. Drug Discov. *13*, 588–602.

Möhrmann, L., Zowada, M.K., Strakerjahn, H., Siegl, C., Kopp-Schneider, A., Krunic, D., Strunk, D., Schneider, M., Kriegsmann, M., Kriegsmann, K., et al. (2020). A perivascular niche in the bone marrow hosts quiescent and proliferating tumorigenic colorectal cancer cells. Int. J. Cancer *147*, 519–531.

Prasetyanti, P.R., and Medema, J.P. (2017). Intra-tumor heterogeneity from a cancer stem cell perspective. Mol. Cancer *16*, 41.

Quereda, V., Bayle, S., Vena, F., Frydman, S.M., Monastyrskyi, A., Roush, W.R., and Duckett, D.R. (2019). Therapeutic Targeting of CDK12/CDK13 in Triple-Negative Breast Cancer. Cancer Cell *36*, 545–558.e7.

Rappsilber, J., Mann, M., and Ishihama, Y. (2007). Protocol for micro-purification, enrichment, pre-fractionation and storage of peptides for proteomics using StageTips. Nat. Protoc. *2*, 1896–1906.

Reaper, P.M., Griffiths, M.R., Long, J.M., Charrier, J.D., Maccormick, S., Charlton, P.A., Golec, J.M., and Pollard, J.R. (2011). Selective killing of ATM- or p53-deficient cancer cells through inhibition of ATR. Nat. Chem. Biol. *7*, 428–430.

Ricci-Vitiani, L., Lombardi, D.G., Pilozzi, E., Biffoni, M., Todaro, M., Peschle, C., and De Maria, R. (2007). Identification and expansion of human colon-cancer-initiating cells. Nature *445*, 111–115.

Sanjana, N.E., Shalem, O., and Zhang, F. (2014). Improved vectors and genome-wide libraries for CRISPR screening. Nat. Methods *11*, 783–784.

Savitski, M.M., Reinhard, F.B., Franken, H., Werner, T., Savitski, M.F., Eberhard, D., Martinez Molina, D., Jafari, R., Dovega, R.B., Klaeger, S., et al. (2014). Tracking cancer drugs in living cells by thermal profiling of the proteome. Science *346*, 1255784.

Schneider, C.A., Rasband, W.S., and Eliceiri, K.W. (2012). NIH Image to ImageJ: 25 years of image analysis. Nat. Methods *9*, 671–675.

Shevchenko, A., Tomas, H., Havlis, J., Olsen, J.V., and Mann, M. (2006). In-gel digestion for mass spectrometric characterization of proteins and proteomes. Nat. Protoc. *1*, 2856–2860.

Shi, W., Oshlack, A., and Smyth, G.K. (2010). Optimizing the noise versus bias trade-off for Illumina whole genome expression BeadChips. Nucleic Acids Res. *38*, e204.

Shin, S.H., Bode, A.M., and Dong, Z. (2017). Addressing the challenges of applying precision oncology. NPJ Precis. Oncol. *1*, 28.

Słabicki, M., Kozicka, Z., Petzold, G., Li, Y.D., Manojkumar, M., Bunker, R.D., Donovan, K.A., Sievers, Q.L., Koeppel, J., Suchyta, D., et al. (2020). The CDK inhibitor CR8 acts as a molecular glue degrader that depletes cyclin K. Nature *585*, 293–297.

Szklarczyk, D., Gable, A.L., Lyon, D., Junge, A., Wyder, S., Huerta-Cepas, J., Simonovic, M., Doncheva, N.T., Morris, J.H., Bork, P., et al. (2019). STRING v11: protein-protein association networks with increased coverage, supporting functional discovery in genome-wide experimental datasets. Nucleic Acids Res. *47* (*D1*), D607–D613.

Toledo, L.I., Murga, M., Zur, R., Soria, R., Rodriguez, A., Martinez, S., Oyarzabal, J., Pastor, J., Bischoff, J.R., and Fernandez-Capetillo, O. (2011). A cell-based screen identifies ATR inhibitors with synthetic lethal properties for cancer-associated mutations. Nat. Struct. Mol. Biol. *18*, 721–727.

van de Wetering, M., Francies, H.E., Francis, J.M., Bounova, G., Iorio, F., Pronk, A., van Houdt, W., van Gorp, J., Taylor-Weiner, A., Kester, L., et al. (2015). Prospective derivation of a living organoid biobank of colorectal cancer patients. Cell *161*, 933–945.

van der Meer, D., Barthorpe, S., Yang, W., Lightfoot, H., Hall, C., Gilbert, J., Francies, H.E., and Garnett, M.J. (2019). Cell Model Passports-a hub for clinical, genetic and functional datasets of preclinical cancer models. Nucleic Acids Res. *47* (*D1*), D923–D929.

Wang, C., Wang, H., Lieftink, C., du Chatinier, A., Gao, D., Jin, G., Jin, H., Beijersbergen, R.L., Qin, W., and Bernards, R. (2020). CDK12 inhibition mediates DNA damage and is synergistic with sorafenib treatment in hepatocellular carcinoma. Gut *69*, 727–736.

Weber, A.M., and Ryan, A.J. (2015). ATM and ATR as therapeutic targets in cancer. Pharmacol. Ther. *149*, 124–138.

Zhang, T., Kwiatkowski, N., Olson, C.M., Dixon-Clarke, S.E., Abraham, B.J., Greifenberg, A.K., Ficarro, S.B., Elkins, J.M., Liang, Y., Hannett, N.M., et al. (2016). Covalent targeting of remote cysteine residues to develop CDK12 and CDK13 inhibitors. Nat. Chem. Biol. *12*, 876–884.

STAR★METHODS

KEY RESOURCES TABLE

REAGENT or RESOURCE	SOURCE	IDENTIFIER
Antibodies		
PE Mouse anti-cleaved PARP (Asp214; clone F21-852)	BD Biosciences	Cat# 552933; RRID: AB_647224
PE Mouse IgG1, κ Isotype Control (clone MOPC-21)	BD Biosciences	Cat# 559320; RRID: AB_397218
Alexa Fluor® 647 Mouse anti-Ki67 (clone B56)	BD Biosciences	Cat# 561126; RRID: AB_10611874
Alexa Fluor® 647 Mouse IgG1 κ Isotype control (clone MOPC-21)	BD Biosciences	Cat# 557783; RRID: AB_396871
Rabbit anti-cleaved PARP (Asp214; clone D64E10)	Cell Signaling Technology	Cat# 5625; RRID: AB_10699459
Rabbit anti-PARP (polyclonal)	Cell Signaling Technology	Cat# 9542; RRID: AB_2160739
Mouse anti-CCNK (polyclonal)	Thermo Fisher Scientific	Cat# A301-939A-M; RRID: AB_2780226
Rabbit anti-CDK12 (7A9-3A3; polyclonal)	Cell Signaling Technology	Cat# 11973; RRID: AB_2715688
Rabbit anti-CDK13 (polyclonal)	Sigma-Aldrich	Cat# SAB2700810; RRID: N/A
Rabbit anti-Phospho-Rpb1 CTD (Ser2; clone E1Z3G)	Cell Signaling Technology	Cat# 13499S; RRID: AB_2798238
Rabbit anti-Phospho-Rpb1 CTD (Ser2/5; polyclonal)	Cell Signaling Technology	Cat# 4735; RRID: AB_2299922
Mouse anti-Rpb1 CTD (clone 4H8)	Cell Signaling Technology	Cat# 2629; RRID: AB_2167468
Rabbit anti-CDK9 (clone C12F7)	Cell Signaling Technology	Cat# 2316; RRID: AB_2291505
Rabbit anti-Mcl1 (polyclonal)	Cell Signaling Technology	Cat# 4572; RRID: AB_2281980
Mouse anti-ATM (clone 2C1 (1A1))	Abcam	Cat# ab78; RRID: AB_306089
Rabbit anti-RAD51 (clone D4B10)	Cell Signaling Technology	Cat# 8875; RRID: AB_2721109
Mouse anti-alpha-Tubulin (clone B-5-1-2)	Sigma-Aldrich	Cat# T5168; RRID: AB_477579
Mouse anti-beta-Actin-Peroxidase (clone AC-15)	Sigma-Aldrich	Cat# A3854; RRID: AB_262011
Rabbit anti-DDB1 (clone D4C8)	Cell Signaling Technology	Cat# 6998S; RRID: AB_10829458
HRP Rabbit anti-Mouse (polyclonal)	Abcam	Cat# ab6728; RRID: AB_955440
HRP Goat anti-Rabbit (polyclonal)	Abcam	Cat# ab6721; RRID: AB_955447
Bacterial and virus strains		
XL10-Gold Ultracompetent Cells	Agilent	Cat# 200315
Sf9 Cells	Thermo Fisher Scientific	Cat# B82501
High Five Cells	Thermo Fisher Scientific	Cat# B85502
Biological samples		
Normal and tumor tissue from CRC patients	Dpt. of General, Visceral and Transplantation Surgery, Heidelberg University Hospital, Heidelberg, Germany, http://kfo227.de/index.php?id=89	N/A
Chemicals, peptides, and recombinant proteins		
Advanced DMEM/F-12	Thermo Fisher Scientific	Cat# 12634028
Glucose	Thermo Fisher Scientific	Cat# 15023021
L-glutamine	Thermo Fisher Scientific	Cat# 25030024
HEPES	Sigma-Aldrich	Cat# H0887
Heparin	Sigma-Aldrich	Cat# H3149

(*Continued on next page*)

Continued

REAGENT or RESOURCE	SOURCE	IDENTIFIER
BSA	PAN-Biotech	Cat# P06-10200
EGF, recombinant human	R&D Systems	Cat# 236-EG
FGF basic, recombinant human	R&D Systems	Cat# 233-FB
RPMI	Thermo Fisher Scientific	Cat# 21875091
FBS	PAN-Biotech	Cat# P40-47500
DMSO	Sigma-Aldrich	Cat# 472301
PFA	Sigma-Aldrich	Cat# P6148
Zombie Green	Biolegend	Cat# 423112
Hoechst 33342	Thermo Fisher Scientific	Cat# H1399
SIGMAFAST Protease Inhibitor Tablets	Sigma-Aldrich	Cat# S8820
NP-40	AppliChem	Cat# A2239
Protease inhibitor complete mini	Roche	Cat# 11836153001
Trypsin, recombinant, Proteomics Grade	Roche	Cat# 3708985001
Empore C18 (Octadecyl) disks, 47mm	Sigma-Aldrich	Cat# 66883-U
TMT10-plex reagents	Thermo Fisher Scientific	Cat# 90110
Phosphatase Inhibitor Cocktail 3	Sigma-Aldrich	Cat# P0044
NuPAGE LDS buffer	Thermo Fisher Scientific	Cat# NP0007
NuPAGE 4 to 12%, Bis-Tris, 1.0 mm, Mini Protein Gel, 12-well	Thermo Fisher Scientific	Cat# NP0322
Reprosil-Pur 120 ODS-3	Dr. Maisch	https://dr-maisch.com
Reprosil-GOLD 120 C18, 3 μm	Dr. Maisch	https://dr-maisch.com
N-Ethylmaleimide	Sigma-Aldrich	Cat# E3876
PBS	Life Technologies	Cat# 14190169, Cas: 128-53-0
Benzonase	VWR International	Cat# 1.01654.0001
4x Laemmli Sample buffer	Bio-Rad	Cat# 1610747
hp-BCD	Sigma-Aldrich	Cat# H107; Cas: 128446-35-5
SbfI	New England Biolabs	Cat# R0642
AsiSI	New England Biolabs	Cat# R0630S
NotI	New England Biolabs	Cat# R0189S
BamHI	New England Biolabs	Cat# R0136
Polybrene	Millipore	TR-1003-G
Protein Assay	Bio-Rad	Cat# 5000001
Mini-Protean TGX pre-cast protein gels (4 – 15%)	Bio-Rad	Cat# 456-1085
Mini-Protean TGX pre-cast protein gels (4 – 20%)	Bio-Rad	Cat# 4561094
PVDF membrane	Bio-Rad	Cat# 162-0174
Western Lightning Plus-ECL substrate	Perkin Elmer	Cat# NEL105001EA
Matrigel® Basement Membrane Matrix High Concentration	Corning	Cat# 354248
NCT01	ENAMINE	Cat# T5321500
NCT02	ENAMINE	Cat# EN300-252755; Cas: 790245-61-3
NCT03	ENAMINE	Cat# T5221761
NCT04	ENAMINE	Cat# T5240492
NCT05	ENAMINE	Cat# T5294311
NCT06	ENAMINE	Cat# T5313340
NCT07	ENAMINE	Cat# T5313685
NCT08	ENAMINE	Cat# T5313686
NCT09	ENAMINE	Cat# T5374800

(*Continued on next page*)

Continued

REAGENT or RESOURCE	SOURCE	IDENTIFIER
NCT10	ENAMINE	Cat# T5414811
NCT11	ENAMINE	Cat# T5265700
NCT12	ENAMINE	Cat# T0504-8673
NCT13	ChemDiv	Cat# V008-4356
NCT14	ChemDiv	Cat# V008-6170
Anisomycin	Sigma-Aldrich	Cat# A9789; Cas: 22862-76-6
NCT02D^{inactive}	Pharmaron, this paper	N/A
NCT02D^{active}	Pharmaron, this paper	N/A
NCT02D^{active} with linker	Pharmaron, this paper	N/A
(R)-MG-132	Tocris	Cat# 6033; Cas: 1211877-36-9
THZ531	Aobious	Cat# AOB8107; Cas: 1702809-17-3
Oxaliplatin	Sigma-Aldrich	Cat# O9512; Cas: 61825-94-3
Irinotecan	Sigma-Aldrich	Cat# I1406; Cas: 136572-09-3
Olaparib (AZD2281)	Selleckchem	Cat# S1060; Cas: 763113-22-0
MLN4924	Hölzel Diagnostika	Cat# HY-70062; Cas: 905579-51-3
Roscovitine	MedChemExpress	Cat# HY-30237 Cas: 186692-46-6
Flavopiridol	Selleckchem	Cat# S1230 Cas: 146426-40-6
Dinaciclib	MedChemExpress	Cat# HY-10492 Cas: 779353-01-4
SR-4835	MedChemExpress	Cat# HY-130250; Cas: 2387704-62-1
Grace's Insect Medium	Thermo Fisher Scientific	Cat# 11605
Fetal bovine serum	Sigma-Aldrich	Cat# F7524
GlutaMAX	Thermo Fisher Scientific	Cat# 35050-038
Pluronic F-68	Thermo Fisher Scientific	Cat#24040
FuGENE® HD Transfection Reagent	Promega	Cat# E2312
FlashBAC GOLD	Oxford Expression Technologies Ltd.	Cat# 100202
Insect Xpress Medium	BioWhittaker	Cat# BE12-730Q
Critical commercial assays		
ATPlite 1step Luminescence Assay System	Perkin Elmer	Cat# 6016736
Ubiquitination Affinity and Control Beads	Cytoskeleton	Cat# UBA01-beads and CUB02-beads
Zombie Green Fixable Viability Kit	Biolegend	Cat# 423111
HumanHT-12 v4 BeadChip	Illumina	Cat# BD-901-1001
AllPrep DNA/RNA/Protein Mini Kit	QIAGEN	Cat# 80004
SureSelectXT Human All Exon V5 + UTR	Agilent	N/A
TruSeq Nano DNA High Throughput Library Prep Kit	Illumina	Cat# 20015965
SureSelect Strand Specific RNA Reagent Kit	Agilent	Cat# G9691B
RNeasy Plus Mini Kit	QIAGEN	Cat# 74134
RevertAid First Strand cDNA Synthesis Kit	Thermo Fisher Scientific	Cat# #K1622
Power SYBR Green PCR Master Mix	Thermo Fisher Scientific	Cat# 4367659
BD Cytofix/Cytoperm Fixation/ Permeabilization Solution Kit	BD Biosciences	Cat# 554714
Pierce Coomassie Plus (Bradford) Assay Kit	Thermo Fisher Scientific	Cat# 23200
Deposited data		
KINOMEscan and Lead Profiling Screen, analyzed data	This paper	Table S3
Differentially expressed genes, Ingenuity® Pathway and Upstream Regulator Analysis, analyzed data	This paper	Table S4

(*Continued on next page*)

Continued

REAGENT or RESOURCE	SOURCE	IDENTIFIER
Cellular Thermal Shift Assay, analyzed data	This paper	Table S5
Pull-down assay results, raw and analyzed data	This paper	Table S5
Whole genome sequencing, raw data	This paper and Giessler et al., 2017	EGA: EGAD00001006263 EGA:EGAD00001006265
Whole exome sequencing, raw data	This paper	EGA: EGAD00001006266
RNA sequencing, raw data	This paper	EGA: EGAD00001006264
Gene expression microarrays, raw data	This paper	EGA: EGAD00010001936
Structure of DDB1 bound to CR8-engaged CDK12-cyclinK	Słabicki et al., 2020	PDB: 6TD3
Fitness Scores of CRC cell lines	Behan et al., 2019	https://score.depmap.sanger.ac.uk
DNA alterations and RNA sequencing data of CRC cell lines	van der Meer et al., 2019	https://cellmodelpassports.sanger.ac.uk
CMS and microsatellite status of CRC cell lines	Linnekamp et al., 2018	N/A
Experimental models: cell lines		
DLD1	Gift from Claudia Scholl (DKFZ Heidelberg)	RRID: CVCL_0248
Colo320	Gift from Claudia Scholl (DKFZ Heidelberg)	RRID: CVCL_1989
Primary human fibroblasts	Gift from Manfred Schmidt (NCT/DKFZ Heidelberg)	N/A
Experimental models: organisms/strains		
NOD.Cg-*Prkdc*^{scid}*Il2rg*^{tm1Wjl}/*SzJ* (NSG) mice	The Jackson Laboratory	RRID: BCBC_4142
Oligonucleotides		
For qPCR primers see Table S6	N/A	N/A
For sgRNA oligos see Table S6	N/A	N/A
BamHI_CDK12_f	AAGGATCCATGCCCAATTCAGAGAGACA	N/A
BamHI_CDK12_r	GCGGCCGCTTATCTCATC	N/A
AsiSI_CCNK-CO_f	GCGATCGCATGAAGGAGAAC	N/A
NotI_CCNK-CO_r	GCGGCCGCTTATCTCATC	N/A
Recombinant DNA		
p602.cPPT.hPGK.IRES.eGFP.WPRE	Gift from Luigi Naldini (San Raffaele Telethon Institute for Gene Therapy, Milan, Italy)	N/A
pLVX.cPPT.CMV.IRES.mCherry.WPRE (pLVX)	Clontech	Cat# 631237
LentiCRISPRv2	Sanjana et al., 2014	Addgene Plasmid# 52961; RRID: Addgene_52961
PGK.CCNK-eGFP.IRES.mCherry.cppt.EF1α.PuroR	Gift from Mikolaj Slabicki (Broad Institute of MIT and Harvard, Cambridge, MA, USA)	N/A
Codon-optimized CCNK cDNA	GenScript	N/A
Software and algorithms		
ACEseq	Giessler et al., 2017	https://github.com/DKFZ-ODCF/ACEseqWorkflow
CMScaller	Eide et al., 2017	https://github.com/peterawe/CMScaller
Ingenuity® Pathway and Upstream Regulator Analysis	QIAGEN	Cat# 830018
STRING Protein-Protein Interaction Networks, Version 11.0	Szklarczyk et al., 2019	https://string-db.org
PRISM, Version 6 and 8	GraphPad	https://www.graphpad.com

(*Continued on next page*)

Continued

REAGENT or RESOURCE	SOURCE	IDENTIFIER
YAPSA	Dieter et al., 2017b	https://www.bioconductor.org/packages/release/bioc/html/YAPSA.html
MaxQuant Software Version 1.5.3.8	Cox et al., 2014	https://www.maxquant.org
ImageJ	Schneider et al., 2012	https://imagej.nih.gov/ij/
SeerSAR	Biosolveit	https://www.biosolveit.de/products/seesar/
FlowJo V10	BD Biosciences	https://www.flowjo.com
Synergyfinder	Ianevski et al., 2019	https://synergyfinder.fimm.fi
Other		
KINOMEscan scanMAX	DiscoveRX	http://www.discoverx.com/home
Lead Profiling Screen 1	Eurofins	https://www.eurofinsdiscoveryservices.com

RESOURCE AVAILABILITY

Lead contact

Further information and requests for resources and reagents should be directed to and will be fulfilled by the Lead Contact, Hanno Glimm (hanno.glimm@nct-dresden.de).

Materials availability

Materials will be made available by the Lead contact. Access to primary cell cultures will require an MTA and is limited to experiments covered by patient consent and the University Ethics Review Board. All reagents used in this study are commercially available, please see the Key Resources Table.

Data and code availability

Raw DNA and RNA sequencing as well as microarray data are deposited at EGA under study ID EGA: EGAS00001004517. They are available upon request if access is granted. To request access, contact DKFZ-HIPO Data Access Committee of Heidelberg Center for Personalized Oncology (hipo_daco@dkfz-heidelberg.de). This paper does not report original code. Any additional information required to reanalyze the data reported in this paper is available from the lead contact upon request.

EXPERIMENTAL MODEL AND SUBJECT DETAILS

Primary CRC TSCs

Human CRC samples were obtained from Heidelberg University Hospital in accordance with the Declaration of Helsinki. Informed consent on tissue collection was received from each patient, as approved by the University Ethics Review Board. Patient characteristics are indicated in Table S1. Tumor sample purification was described previously (Dieter et al., 2011; Möhrmann et al., 2020). TSCs were cultivated in ultra-low attachment flasks (Corning) in serum-free medium (Advanced DMEM/F-12 supplemented with 0.6% glucose, 2 mM L-glutamine [all Thermo Fisher Scientific], 5 mM HEPES, 4 μg/mL heparin [both Sigma-Aldrich], and 4 mg/mL bovine serum albumin [PAN-Biotech]). Growth factors (20 ng/mL EGF and 10 ng/mL FGF basic [both R&D Systems]) were added twice per week.

TSCs and cell lines were authenticated using Multiplex Cell Authentication and purity of TSCs was validated using the Multiplex cell contamination test (Multiplexion). No Mycoplasma, SMRV or interspecies contaminations were detected. Purity of established cultures was monitored to assure pure epithelial cell content and exclude contaminations with hematopoietic or stroma cells as described before (Dieter et al., 2017a).

CRC cell lines

DLD1 and Colo320 cells were a kind gift from Claudia Scholl (DKFZ Heidelberg) and cultured in RPMI supplemented with 10% fetal bovine serum (FBS) and 1% L-glutamine.

Mice models

Female eight- to ten-week-old NOD.Cg-*Prkdc*^{scid}*Il2rg*^{tm1Wjl}/*SzJ* (NSG) mice were used in this study, obtained from the Jackson Laboratory and housed at a specific-pathogen-free animal facility according to all applicable laws and regulations subsequent to approval by the institution's animal care and ethical committee.

METHOD DETAILS

DNA- and RNA-sequencing of TSCs

Patient tumors, matched healthy tissue and TSCs were processed by the Sample Processing Lab of the DKFZ Heidelberg. DNA and RNA were extracted using standard kits (QIAGEN). Library preparation was performed with standard kits for whole genome, whole exome or mRNA sequencing (Agilent, Illumina or New England Biolabs) and libraries were sequenced on a HiSeq2000, HiSeq2500 or HiSeqX (Illumina). Reads from DNA- and RNA-sequencing were mapped to the 1000 Genomes Phase II assembly of the human reference genome (NCBI build 37.1). Single-nucleotide variants and small insertions/deletions were analyzed using a previously reported bioinformatics workflow (Dieter et al., 2017b). ACEseq was used to identify copy number aberrations, loss of heterozygosity as well as tumor cell content and ploidy of a sample (Giessler et al., 2017). Losses and gains were defined as described before (Horak et al., 2020). The contributions of mutational signatures were calculated by the R/Bioconductor package YAPSA according to Alexandrov-COSMIC signatures (https://cancer.sanger.ac.uk/cosmic/signatures_v2) (Alexandrov et al., 2013; Dieter et al., 2017b; Ma et al., 2018). Molecular stratification was performed on RNA-sequencing and microarray data using the R package CMScaller (Eide et al., 2017). Gene expression data that could not be assigned using CMScaller were stratified using signatures from Linnekamp et al. (2018). Sequencing and microarray data have been deposited at the European Genome-phenome Archive as EGA: EGAS00001004517.

High-throughput compound screen on TSC cells

For compound screening, 3000 TSC cells were plated per well of 384-well plates (Perkin Elmer) 24 h prior to addition of compounds and cultivated in standard culture conditions. Cells were treated with compounds for 96 h and viability was measured afterward using the ATPLite assay (Perkin Elmer). Anisomycin (5 μM) was used as positive control. The assay was validated against a pilot library, a representative sample of 4,080 compounds, at a final concentration of 10 μM in two independent experiments.

The DKFZ/EMBL library was assembled selecting 78,600 compounds (including pilot library) with diverse chemical scaffolds from commercial vendors (Enamine, ChemDiv and ChemBridge) and was screened in the final screen against TSC03 cells. Positive and negative controls in the library were defined based on results across previously screened cell lines. Results were calculated as percent growth inhibition and the activity threshold was set at > 95%. Actives were clustered by chemical similarity into families. In the selection process, compounds from such families were prioritized over singletons. Considering previous cytotoxicity data (MCF7; data not shown) 120 compounds were selected for further analysis.

The selected compounds were tested in 11-point dose responses in the viability assay and in a counter-screen with ATP (included in the ATPlite assay). 14 compounds with $IC_{50} < 20$ μM, appropriate dose responses (Hill slope between 0.5 and 2.5) and lack of interference with ATP were selected for further evaluation in additional TSCs and non-malignant control cells. This resulted in a single compound that showed a differential response. An overview of the triaging process is given in Figure 1E.

Individual drug assays

For compound validation experiments, TSC cells were seeded as in the final screen and after one day cells were treated with 10-point dilutions of compounds. Cells were incubated with the compounds for 72 h or 96 h before viability was measured at least in triplicates using the ATPlite assay. Prism Version 6, 8 or 9 were used to generate dose-response curves and to calculate IC_{50} values, using DMSO- and Anisomycin-treated cells as negative and positive controls, respectively. Calculated IC_{50} values above 50 μM were set to 50 μM according to the highest used concentration.

Drug competition assays

For competition assays, cells were treated with the competitive compound (THZ531, Flavopiridol, Roscovitine, Dinaciclib) 15 min before NCT02 was added for 2 h. Degradation of CCNK was measured using a reporter as described before (Słabicki et al., 2020) and quantified by flow cytometry using a FACSAria (BD Biosciences).

Synergy assessment

For synergy assessment, drug assays using serial dilutions of oxaliplatin or irinotecan in combination with fixed doses of NCT02 were done as described above with the modification that cells were treated already 4 h after seeding. Synergy was calculated based on the Bliss reference model using Synergyfinder (accessed via https://synergyfinder.fimm.fi) (Ianevski et al., 2019).

In vitro biochemical profiling of NCT02

Profiling of NCT02 against a panel of 468 kinases was performed by DiscoverX using the KINOMEscan scanMAX assay. Interaction of NCT02 with 68 critical targets was tested by Eurofins using the Lead Profiling Screen 1.

Analysis of differentially expressed genes

Gene expression levels were determined for 9 sensitive and 6 intermediate-sensitive/resistant TSCs treated with 3 μM NCT02 or DMSO for 12 h using HumanHT-12 V4 R2 Expression BeadChips (Illumina) at the Genomics and Proteomics Core Facility of DKFZ Heidelberg. To achieve a more balanced distribution between sensitive and resistant TSCs for statistical analysis

intermediate-sensitive and resistant TSCs were grouped together as resistant. To remove non-specific signal, background correction and quantile normalization using control probes was implemented (Shi et al., 2010). Probes that failed to reach a detection *p-value* of 0.05 on more than 90% of arrays were filtered as 'not expressed'. Resulting data were log2 transformed. For identification of significantly over- and underrepresented genes a linear regression model using the two IC_{50} categories 'sensitive' and 'resistant' was applied based on the median IC_{50} value of each culture and a cutoff value of 4 μM. The Benjamini-Hochberg correction was applied in order to control the false discovery rate.

Ingenuity® pathway and upstream regulator analysis

The list of genes significantly differentially expressed in sensitive TSCs after treatment with NCT02 (adjusted *p-value* < 0.01) was uploaded for Ingenuity® pathway analysis (QIAGEN) and all mapped genes were analyzed using Core Analysis to identify significantly affected canonical pathways based on right-tailed Fisher's exact test. To predict upstream molecules which may cause the observed gene expression changes Upstream Regulator Analysis was performed using the same gene set. An overlap *p-value* was calculated using Fisher's exact test and activation z-scores were determined to predict activation or inhibition of the regulators.

qRT-PCR

Total RNA was obtained using the RNeasy plus mini kit (QIAGEN). 1 μg of RNA was reverse transcribed using the RevertAid First Strand cDNA Synthesis Kit (Thermo Fisher Scientific). qRT-PCR was performed with the Power SYBR™ Green PCR Master Mix (Applied Biosystems) and analyzed using LightCycler 480 (Roche). Relative expression values for each gene of interest were obtained by normalizing to GAPDH or beta-Actin mRNA expression using the ΔΔCt method.

γH2AX staining

Cells were treated with NCT02 or DMSO as indicated and afterward fixed in 4% PFA on ice, spun down and resuspended in cold Cytofix/Cytoperm Fixation/Permeabilization Solution (BD Biosciences). After 5 min incubation on ice, cells were centrifuged, washed once with Perm/Wash buffer (Cytofix/Cytoperm kit) and incubated with Alexa Fluor® 647 anti-H2A.X (Ser139) antibody (Biolegend, Cat# 613408) or isotype control (Biolegend, Cat# 400136) for 30 min at room temperature (RT). Afterward, cells were washed once with Perm/Wash buffer, once with cold PBS and analyzed using an LSR II or Aria flow cytometer (BD Biosciences). At least 10,000 events were recorded.

Spheroid formation assays

To test activity of NCT02 against SFCs TSC cells were treated with NCT02 or DMSO as indicated, dissociated to a single-cell suspension and sorted into ultra-low attachment 96-well plates (Corning) using a FACSAria II Cell Sorter (BD Biosciences). Sorting efficiency was confirmed microscopically. Wells containing single cells after sorting were monitored for up to 21 days and wells with spheroid formation were quantified.

Analysis of cell cycle and apoptosis

For cell cycle analysis, TSC cells were treated with NCT02 or DMSO as indicated. Afterward, cells were dissociated, stained for live cell/dead cell discrimination with Zombie Green (BioLegend) for 15 min at RT and washed with Cell Staining Buffer (BioLegend) according to manufacturer's instructions. Cells were resuspended in cold permeabilization buffer (320 mM sucrose, 5 mM $MgCl_2$, 10 mM HEPES, 1% Triton X-100, pH 7.4), gently vortexed and kept on ice for 5 min. After centrifugation, cells were washed twice with wash buffer (320 mM sucrose, 5 mM $MgCl_2$, 10 mM HEPES, pH 7.4) and stained with Alexa Fluor® 647 mouse anti-Ki67 antibody (BD Biosciences, Cat# 561126) or isotype control (BD Biosciences; Cat# 557783) for 30 min at RT in staining buffer (320 mM sucrose, 5 mM $MgCl_2$, 10 mM HEPES, 1% BSA, 0.1% NaN_3, pH 7.4). Next, DNA was stained with Hoechst 33342 (Thermo Fisher Scientific) for 10 min in staining buffer. After one further washing step with PBS cells were analyzed using an LSR II flow cytometer. At least 10,000 events were recorded and single Zombie Green negative cells were assigned to cell cycle phases based on DNA content. Ki67-signal allowed discrimination of G0 and G1 phases, but was not used for final analysis.

For apoptosis analysis, TSC cells were treated with NCT02 or DMSO as indicated. Subsequently, cells were dissociated, fixed with 4% PFA for 15 min at RT and washed with cold PBS. Next, cells were resuspended in permeabilization buffer, gently vortexed and incubated on ice for 5 min. Cells were washed twice with staining buffer, resuspended in staining buffer containing PE Mouse anti-cleaved PARP antibody (BD Biosciences; Cat# 552933) or isotype control (BD Biosciences; Cat# 559320) and incubated on ice for 30 min. After one further washing step with PBS cells were analyzed using an LSR II flow cytometer. At least 10,000 events were recorded and single $cPARP^+$ cells were quantified.

Thermal proteome profiling

Thermal proteome profiling was used to study the thermal stabilization of potential drug targets after compound binding. The overall experimental setup has been described previously (Jafari et al., 2014; Martinez Molina et al., 2013; Savitski et al., 2014). For each condition, 3×10^7 TSC03 cells were incubated in the presence of NCT02, $NCT02D^{inactive}$ or DMSO (2 h, 10 μM) in duplicates. After incubation samples were washed twice with PBS and resuspended in PBS/1X protease inhibitor (Sigma-Aldrich). Each sample was separated into 10 aliquots and transferred to PCR tubes (2.5×10^6 cells/condition). Subsequently, aliquots were heated to different

temperatures using a PCR-cycler (FlexCycler2, Jena Bioanalytik; temperature steps: 40.0, 42.9, 46.0, 49.6, 53.2, 56.8, 60.4, 64.0, 67.1, 70.0°C). After heating aliquots were incubated for 3 min at RT. For cell lysis, NP-40 (final concentration 0.4% [w/v]) was quickly added to each aliquot followed by 6 - 7 freeze/thaw cycles using liquid N_2 and a water bath at 25°C. Subsequently, aliquots were transferred to ultracentrifuge tubes and centrifuged at 100,000 g (4°C, 20 min). After transferring the supernatant of each aliquot to a fresh tube, the protein concentration was determined using Pierce Coomassie Plus (Bradford) Assay Kit (Thermo Fisher Scientific). Reduction and alkylation of equal volumes per sample were carried out for 15 min at 37°C in urea buffer (8 M urea, 50 mM TEAB (pH 8.5), 1x protease inhibitor complete mini (Roche), 10 mM TCEP, 40 mM CAA), followed by three-times dilution with 50 mM TEAB, pre-digestion for 2 h at 37°C with trypsin (recombinant, Proteomics Grade, Roche Diagnostics GmbH; protease:protein ratio of 1:100) and overnight-digestion at 37°C with trypsin (recombinant, Proteomics Grade, Roche Diagnostics GmbH; protease:protein ratio of 1:100). Afterward, a desalting step of the acidified, tryptic digests with C18 StageTips (in-house preparation; material: Empore C18 (Octadecyl) disks, 47mm [Sigma-Aldrich]) (Rappsilber et al., 2007) was performed followed by labeling of the peptides with TMT10-plex reagents (Thermo Fisher Scientific) in 50 mM TEAB (pH 8.5) for 1 h. TMT-labeled samples were mixed by combining all 10 temperature steps per condition in one TMT10-plex experiment. A further desalting step with C18 Sep-Pak cartridges was followed by peptide fractionation via hydrophilic strong anion exchange chromatography (hSAX; Dionex Ultimate 3000 system; column: Dionex Ion Pac AS24 [Thermo Fisher Scientific]; trap: Dionex IonPac AG24 [Thermo Fisher Scientific]; 5 mM Tris-HCl pH 8.5 [buffer A], 5 mM Tris-HCl pH 8.5, 1 M NaCl [buffer B]) and another desalting step using C18 StageTips. 40 fractions were collected and pooled into 24 fractions for LC-MS/MS analysis.

Chemical proteomics

TSC03 cells (3×10^7 cells per condition, each in triplicates) were treated in culture for 2 h with 10 μM NCT02 and mock (0.1% DMSO), respectively, and washed with PBS before harvest. Cell pellets were lysed by adding a mild lysis buffer keeping proteins in their native fold and retaining protein-protein interactions. Protein pulldowns were performed as described (Médard et al., 2015). In short, for cell lysis 600 μL compound pull down (CP) buffer (50 mM Tris/HCl, pH 7.5, 5% glycerol, 1.5 mM $MgCl_2$, 150 mM NaCl, 25 mM NaF, 1 mM sodium ortho-vanadate, 0.8% NP-40, 1 mM DTT) containing protease inhibitor (SigmaFast protease inhibitor tablet, Sigma-Aldrich) and phosphatase inhibitors (Phosphatase Inhibitor Cocktail 3, Sigma-Aldrich) was added to the cell pellets. Cells were frozen and after thawing subjected to ultracentrifugation (> 100,000 g, 4°C, 1 h). Protein concentration of the cleared lysate was determined and each sample was brought to 5 mg/mL (4 mg total protein amount) by adding CP buffer. Samples were further diluted with CP buffer without NP-40 to reduce the concentration of NP-40 to 0.4%. Once again the lysates were cleared by ultracentrifugation (20 min, 4°C, 52,000 g) and supernatants were used for pulldown experiments. The amino linkable compound $NCT02D^{active}$ was coupled to NHS-Sepharose beads according to Médard et al. (2015), and beads were equilibrated with CP buffer containing 0.4% NP-40 (CP-0.4). Lysates were incubated with 35 μL settled beads each for 30 min at 4°C (head-over-end shaker). Beads were washed with 3 mL CP-0.4 buffer followed by a washing step with 2 mL CP buffer/0.2% NP-40. Proteins were eluted from the beads by incubation with 2X NuPAGE LDS buffer (Thermo Fisher Scientific) containing 50 mM DTT for 30 min, 50°C, 700 rpm. The supernatant was alkylated (55 mM chloroacetamide in H_2O, 30 min, room temperature) and each protein sample was loaded on a 10 well Bis/Tris Gel (NuPAGE, 4%–12%, Thermo Fisher Scientific). SDS-PAGE was performed for 5 min at 200 V to transfer the sample into the gel. In the following in-gel digestion was performed of the full sample lane following standard protocols (Shevchenko et al., 2006). Before LC-MS/MS analysis, peptide samples were desalted using C18 StageTips. A third of each sample was analyzed by LC-MS/MS analysis.

LC-MS/MS analysis

Nanoflow LC-MS/MS analysis of peptide samples was performed on an UltiMate 3000 RSLCnano System (Thermo Fisher Scientific) coupled to a Q-Exactive Plus mass spectrometer (Thermo Fisher Scientific). Peptides were delivered to a trap column (75-μm inner diameter × 2 cm, packed with 5-μm C18 resin (Reprosil-Pur 120 ODS-3, Dr. Maisch) at a flow rate of 5 μL/min for 9 min in 100% solvent A (0.1% FA in HPLC-grade water, 5% DMSO). After loading and washing, peptides were transferred to an analytical column (75 μm × 55 cm C18 column; Reprosil-GOLD 120, 3 μm, Dr. Maisch, Germany) and separated using a linear gradient of 110 min ramping from 4% to 32% solvent B (0.1% FA, 5% dimethyl sulfoxide in ACN) at a flow rate of 300 nL/min. 5% (v/v) DMSO were used in solvent A and B to boost the nanoelectrospray response (Hahne et al., 2013). Peptides were detected (MS1, 70K resolution) and sequenced/quantified (MS2) in the Orbitrap using higher-energy collisional dissociation (HCD) fragmentation. For TMT-labeled CETSA samples, MS2 resolution has been set to 35K in combination with a target value of 2e5 ions and an isolation window of 1.2 Th. Label-free pulldown samples were measured with 17.5K MS2 resolution, 1e5 target value and an isolation window of 1.7 Th.

Processing of LC-MS/MS data was conducted using MaxQuant Software (Version 1.5.3.8) (Cox et al., 2014). For TPP analysis, resulting quantitative data was analyzed using "TPP" R package (Franken et al., 2015) as described (Savitski et al., 2014). For target candidate selection the following criteria of the "TPP" results had to be fulfilled: Min p value < 0.4 (Benjamini-Hochberg corrected); ΔTm of R1 and R2 have same sign; ΔTm (drug versus DMSO) > ΔTm (DMSO R1 versus DMSO R2); Min slope less than - 0.06.

Data analysis of the pull-down experiments was performed in a label-free manner based on the LFQ algorithm included in the MaxQuant software. Only proteins were considered that were detected with at least three unique peptides in mock treated replicates. Standard t test was performed to identify significant outlier proteins between triplicates of compound and mock treatment.

For visualization of known protein-protein interactions, target candidates from TPP with significant ΔTm were uploaded to https://string-db.org (Szklarczyk et al., 2019).

Synthesis of derivatives

During a first structure-activity relationship (SAR) exploration of the lead molecule NCT02 a very high structural variability at the northern bezofuranderivative part of the molecule was encountered, while the southern triazole part showed a very steep SAR. Only small variations like replacement of the 5-methyl substituent with ethyl or trifluoromethyl were tolerated, whereby other heterocycles or substituent patterns led to inactive compounds (data not shown). In a next step we synthesized several combinations of the best northern parts with the 5-trifluormethyl-thiazole. This approach led us among others to the active compound NCT02D, which showed a similar selectivity profile than the compound NCT02 (Figure S2). For use of the compound in pull-down assays we had to attach a suitable linker to our molecule without losing the activity or selectivity. With more freedom for variations at the northern part we decided to attach the required linker at the Aniline part of NCT02D^{active}.

Synthesis of derivatives was performed by Pharmaron (Waltham, MA). For synthesis of NCT02D^{inactive} (Figure S2) (E)-ethyl 3-(5,6,7,8-tetrahydronaphtho[2,3-b]furan-2-yl)acrylate (40 mg, 0.148 mmol) was hydrogenated with palladium (0.63 mg, 0.006 mmol) in 2 mL methanol to give 40 mg (95%) of ethyl 3-(5,6,7,8-tetrahydronaphtho[2,3-b]furan-2-yl)propanoate as colorless oil. MS (ESIpos): m/z = 273 (M+H)+. Ethyl 3-(5,6,7,8-tetrahydronaphtho[2,3-b]furan-2-yl)propanoate (40 mg, 0.15 mmol) was saponificated with lithium hydroxide monohydrate (30 mg, 0.73 mmol) in water/THF to give 35 mg of the corresponding acid as yellow solid MS (ESIpos): m/z = 245 (M+H)+. 3-(5,6,7,8-tetrahydronaphtho[2,3-b]furan-2-yl)propanoic acid (35 mg,0.14 mmol), were coupled to 5-methylthiazol-2-amine (16.4 mg, 0.14 mmol) with 2-(1H-Benzotriazole-1-yl)-1,1,3,3-tetramethyluronium tetrafluoroborate (55.19 mg, 0.17 mmol) as described for NCT02D to give 16.1 mg (32%) of the final product as an off-white solid. MS (ESIpos): m/z = 341 (M+H)+.

For synthesis of NCT02D^{active} (Figure S2) 2-(4-(Dimethylamino)phenyl)acetic acid (300 mg, 1.62 mmol) 5-(trifluoromethyl)thiazol-2-amine (273 mg, 1.62 mmol) and triethylamine (0.68 mL, 4.87 mmol), were dissolved in 15 mL of dichloromethane. 2-(1H-Benzotriazole-1-yl)-1,1,3,3-tetramethyluronium tetrafluoroborate (625 mg, 1.95 mmol) was added at 0°C under nitrogen. The resulting solution was stirred at room temperature for 22 h. The reaction mixture was evaporated to dryness and the residue was purified by flash chromatography (Hexane/ethyl acetate gradient). The solvent was evaporated under reduced pressure to yield 251 mg (46%) of the final compound as a white solid. MS (ESIpos):m/z = 330 (M+H)+. 1H NMR (400 MHz, CHLOROFORM-d) δ ppm 2.98 (s, 6 H) 3.77 (s, 2 H) 6.66 - 6.80 (m, 2 H) 7.09 - 7.18 (m, 2 H) 7.61 - 7.76 (m, 1 H) 9.09 - 9.27 (m, 1 H).

For synthesis of NCT02D^{active} with linker (Figure S3) Buchwald-Hartwig coupling of tert-butyl 2-(2-(2-aminoethoxy)ethoxy)ethylcarbamate (434 mg, 1.74 mmol) and methyl 2-(4-bromophenyl)acetate (400 mg, 1.74 mmol) using BrettPhos palladium(II) biphenyl-2-amine mesylate (158 mg, 0.17 mmol), cesium carbonate (1.71 mg, 5.24 mmol), and BrettPhos (94 mg, 0.17 mmol), yielded 550 mg (72%) of methyl {4-[(2,2-dimethyl-4-oxo-3,8,11-trioxa-5-azatridecan-13-yl)amino]phenyl} acetate as a yellow oil. MS (ESIpos): m/z = 397 (M+H)+. Methyl {4-[(2,2-dimethyl-4-oxo-3,8,11-trioxa-5-azatridecan-13-yl)amino]phenyl}acetate (550 mg, 1.2 mmol), was methylated with potassium carbonate (518 mg, 3.7 mmol), and iodomethane (354 mg, 2.5 mmol) to give 460 mg (74%) of methyl {4-[(2,2-dimethyl-4-oxo-3,8,11-trioxa-5-azatridecan-13-yl)(methyl)amino]phenyl}acetate as a yellow oil. MS (ESIpos):m/z = 411 (M+H)+. Methyl {4-[(2,2-dimethyl-4-oxo-3,8,11-trioxa-5-azatridecan-13-yl)(methyl)amino] phenyl}acetate (460 mg, 0.9 mmol), was saponificated with lithium hydroxide to give 280 mg (69%) of the corresponding acid as yellow oil. MS (ESIpos):m/z = 397 (M+H)+. {4-[(2,2-dimethyl-4-oxo-3,8,11-trioxa-5-azatridecan-13-yl)(methyl)amino]phenyl}acetic acid (280 mg, 0.64 mmol), and 5-(trifluoromethyl)thiazol-2-amine (128 mg, 0.76 mmol), were dissolved in 5 mL of dichloromethane, then 4-(4,6-dmethoxy-1,3,5-triazine-2-yl)-4-methyl morpholinium chloride (334 mg, 1.27 mmol), was added and the resulting mixture was stirred at room temperature for 13 h. The resulting mixture was diluted with water and extracted with dichloromethane, the organic phase was washed with water, brine, dried over anhydrous sodium sulfate and concentrated under vacuum, the residue was purified with silica gel column chromatography (ethyl acetate /petroleum ether 1:1) to give 150 mg of the product as a light yellow solid. MS (ESIpos):m/z = 547 (M+H)+. Boc deprotection using trifluoroacetic acid (0.3 mL) in dichloromethane gave 12.9 mg of the final product as an off-white solid. MS (ESIpos):m/z = 447 (M+H)+. ^{1}H NMR (400 MHz, DMSO-d6) δ ppm 2.70 (br t, J = 5.62 Hz, 2 H) 2.89 (s, 3 H) 3.38 (t, J = 5.69 Hz, 2 H) 3.44 - 3.61 (m, 10 H) 6.65 (d, J = 8.68 Hz, 2 H) 6.98 - 7.17 (m, 2 H) 7.86 - 7.99 (m, 1 H).

Rescue experiments using CCNK/CDK12-overexpression

The coding sequence of the human *CDK12* gene (ENSG00000167258; NCBI Gene ID: 51755) was amplified from RNA isolated from a TSC using specific primers (BamHI_CDK12_fwd and SbfI_CDK12_rev), cloned into the p602.cPPT.hPGK.IRES.eGFP.WPRE plasmid (p602-CDK12; gift from Luigi Naldini, San Raffaele Telethon Institute for Gene Therapy, Milan, Italy) using the restriction enzymes BamHI and SbfI (New England Biolabs) and verified by sequencing. The coding sequence of the human *CCNK* gene (ENSG00000090061; NCBI Gene ID: 8812) was amplified from a codon-optimized (CO) cDNA clone (GenScript) using specific primers (AsiSI_CCNK-CO_fwd and NotI_CCNK-CO_rev). The CMV promoter in the pLVX.cPPT.CMV.IRES.mCherry.WPRE vector (Clontech; plasmid# 631237) was replaced by the hPGK promoter to generate the pLVX.cPPT.hPGK.IRES.mCherry.WPRE (pLVX) destination vector. CCNK-CO was transferred into pLVX (pLVX-CCNK) using the restriction enzymes AsiSI and NotI (New England Biolabs) and verified by sequencing.

Concentrated lentivirus production was performed as described previously (Follenzi et al., 2000). For the generation of CCNK/CDK12 co-overexpressing cells, TSC03 cells were transduced in a stepwise process using unconcentrated lentivirus (pLVX-CCNK and pLVX virus) and concentrated lentivirus with a multiplicity of infection of 10 (p602-CDK12 and p602), both times in the presence of 8 μg/mL polybrene. Double positive mCherry+/eGFP+ cells (pLVX-CCNK/p602-CDK12 and pLVX/p602) were sorted using a FACSAria II Cell Sorter. Overexpression was confirmed at protein level and monitored based on mCherry/eGFP-signal.

Western blots

For protein isolation TSC cells were lysed in an appropriate volume of lysis buffer (20 mM Tris-HCl (pH 7.5), 150 mM NaCl, 10 mM NaF, 1% Triton X-100). Protein concentration was measured using Bio-Rad Protein Assay (Bio-Rad) or Pierce BCA protein assay kit (Thermo Fisher Scientific) and adjusted to 10 to 50 μg per line, using 4X Laemmli Sample Buffer with the addition of 10% 2-mercaptoethanol (all Bio-Rad). Samples were run on 4 – 15% or 4 - 20% Mini-Protean® TGX pre-cast protein gels and transferred to PVDF membranes using the Trans-Blot Turbo Transfer System (all Bio-Rad). Membranes were blocked for 1 h at RT using 5% milk in TBS-T (20 mM Tris-HCl pH 7.5, 150 mM NaCl, 0.1% Tween20), residual blocking buffer was removed and membranes were incubated in primary antibody at 4°C over night. After repeated washing, membranes were incubated with secondary antibody at RT for 1 h. For imaging, blots were incubated in Western Lightning Plus-ECL substrate (Perkin Elmer) and developed using the ChemiDoc XRS+ Imaging System (Bio-Rad). Bands were quantified using ImageJ (Schneider et al., 2012).

Rescue experiments using inhibitors of proteasome or ubiquitin ligases

1 - 2 × 10^6 TSC cells were seeded per well of an ultra-low attachment 6-well plate (Corning). The next day, cells were treated with 10 μM MG132 (Tocris) or DMSO for 2 h, followed by co-treatment with 10 μM NCT02 or DMSO for additional 6 h. Afterward, 1 mL of cell suspension was harvested for western blot and remaining cells were seeded for viability assays 24 and 48 h later using the ATPlite assay. For inhibition of Cullin-RING E3 Ubiquitin ligases, cells were co-treated 24 h after seeding with 10μM NCT02 and 10 μM MG132 or 100 nM MLN4924 (Hölzel Diagnostika) for 6 h.

Ubiquitin immunoprecipitation

24 h after seeding, 6 × 10^7 cells were treated with 10 μM MG132 or DMSO for 2 h, followed by co-treatment with 10 μM NCT02 or DMSO for additional 6 h. Afterward, cells were collected by centrifugation and washed twice with 20 mM N-Ethylmaleimide (NEM; MP Biomedicals) in ice-cold PBS (Life Technologies). Cell pellets were lysed in 500 μL of ice-cold TUBE buffer (50 mM Tris-HCl (pH 7.5), 150 mM NaCl, 1 mM EDTA, 1.0% NP40, 10% glycerol) supplemented with 25X protease inhibitor (Roche), 20 mM NEM and 137.5 units of Benzonase (VWR International), and stored at −80°C overnight. Cell pellets were thawed on ice and rotated at 4°C for 30 min, followed by 10 min centrifugation at 4°C and collection of the supernatant. 25 μL per sample were taken as input control and the remaining was used for the pull-down assay.

Ubiquitin Affinity Control Beads and Ubiquitin Affinity Beads 1 (Cytoskeleton) were reconstituted according to manufacturer instructions. 20 μL of beads slurry was added per sample. After 2.5 h incubation in constant rotation at 4°C, the beads were pelleted by centrifugation and washed three times with cold TBS-T. After the last centrifugation step, the supernatant was removed and 25 μL of 4X Laemmli buffer (Bio-Rad) was added to the pellets. Beads were incubated at 95°C for 5 min and the supernatant was transferred to a fresh tube containing 1 μL of 2-mercaptoethanol. The samples were incubated again 5 min at 95°C and used for WB.

Quantification of CCNK degradation using the CCNK-eGFP reporter

The PGK.CCNK-eGFP.IRES.mCherry.cppt.EF1α.PuroR CCNK-stability reporter was a gift from Mikolaj Slabicki (Broad Institute of MIT and Harvard, Cambridge, MA, USA) (Słabicki et al., 2020). Lentivirus was produced, DLD1 cells infected and selected as described (Li et al., 2021). Using FlowJo (BD Biosciences), the geometric mean of the eGFP and mCherry fluorescent signal for living cells was calculated. The ratio of eGFP to mCherry was normalized to the average of three DMSO-treated controls. For measuring CCNK degradation in CRISPR/Cas9-modified DLD1 cells that contained the puromycin-resistance cassette and could not be selected again, the geometric mean of the eGFP and mCherry fluorescent signal for living and $mCherry^{high}$ cells was used for analysis.

Co-immunoprecipitation of CCNK/CDK12 with FLAG-DDB1

Protein purification of DDB1

Flag-TEV-DDB1 (2-1140, Uniprot: Q16531) was expressed in 4 L Trichoplusia ni High Five insect cell culture transfected with baculovirus (Invitrogen) at multiplicity of infection (MOI) 1.0 for 48 h at 27°C. After resuspension in 50 mM Tris/HCl pH 7.5, 500 mM NaCl, 10% Glycerol, 1 mM TCEP, Complete Protease Inhibitor Cocktail EDTA-free, 0.1% NP40 and centrifugation at 25,000 g for 60 min at 4°C the supernatant was incubated with Anti-FLAG agarose (Anti-FLAG M2 Affinity Gel; Sigma-Aldrich) overnight at 4°C. After washing with buffer A (50 mM Tris/HCl pH 7.5, 500 mM NaCl, 10% Glycerol, 1mM TCEP) the protein was eluted by adding buffer A, supplemented with 150 μg/mL Flag Peptide (Sigma-Aldrich). The protein was gelfiltrated on a S200 26/60 column (GE Healthcare) with buffer A. The relevant peak fraction was pooled, concentrated, frozen in liquid nitrogen and stored at − 80°C.

Protein purification of the CDK12 complex

The CDK12 complex, consisting of His-Tev-CDK12 (715-1052, Uniprot: Q9NYV4) and CCNK (11-267, Uniprot: O75909) was expressed in 8 L Trichoplusia ni High Five insect cell culture, which was transfected with baculoviruses (MOI 1, MOI 0.5 and MOI

0.5 for CDK12, CCNK and CAK1 (1-368), respectively) for 48 h at 27°C. After resuspension in lysis buffer (50 mM HEPES pH 7.5, 400 mM NaCl, 5% Glycerol, 1 mM DTT, Complete Protease Inhibitor Cocktail EDTA-free, 0,5% NP40, Benzonase, 40 mM Imidazole) and centrifugation at 27,500 g for 60 min at 4°C the complex was affinity-purified via a 5 mL, HisTrapHP column (GE Healthcare). The column was washed with buffer A (50 mM HEPES pH 7.5, 400 mM NaCl, 5% Glycerol, 1mM DTT, 40 mM Imidazole) and the complex was cleaved from the column by applying TEV protease (TEV / Protein ratio of 1:10) overnight at 6°C. Elution was performed with buffer A, and the complex was subjected to size exclusion chromatography (SEC) Superdex75 26/60 column (GE Healthcare) equilibrated with buffer A.

The relevant peak fraction was pooled, concentrated, frozen in liquid nitrogen and stored at − 80°C.

Co-immunoprecipitation assay

Anti-FLAG M2 agarose beads (80 μL, Anti-FLAG M2 Affinity Gel; Sigma-Aldrich) in Pierce Spin Columns were equilibrated with reaction buffer (10 mM HEPES pH 7.4, 150 mM NaCl, 0.005% v/v Surfactant P20, 1 mM DTT, 1 mg/mL BSA). The beads were incubated with purified Flag-tagged DDB1, untagged CDK12/CCNK together with compound (THZ531, CR8, SR-4835, NCT02) in equimolar concentrations of 5 μM for 1 h while shaking. A negative control (DMSO only) was included in the assay. After washing with reaction buffer three times, the bound protein was eluted with reaction buffer, supplemented with 300 μg/mL Flag-peptide for 30 min. All assay steps were performed at 4°C. The eluted samples were analyzed by SDS-PAGE and stained with Coomassie blue.

In silico-modeling of NCT02 binding mode

To generate a model of NCT02 binding to CDK12 the software SeeSAR (Biosolveit) was used. Initially a binding pocket was defined to include all residues lining both the CDK12 ATP binding site and the adjacent DDB1 binding pocket in the CDK12/CCNK/DDB1 complex structure (PDB: 6TD3) (Słabicki et al., 2020). 100 poses for NCT02 binding were generated and all were evaluated using the built-in HYDE scoring function in combination with manual inspection. The pose with the most probably binding mode was selected for further analysis.

CRISPR/Cas9 editing

Individual sgRNAs were cloned into the lentiCRISPRv2 vector (gift from Feng Zhang [Addgene, plasmid #52961]) as described (Sanjana et al., 2014). For viability assays with knock-out cell lines, the vector was modified by replacement of the puromycin-resistance cassette with eGFP. 4 × 10^5 Colo320 and 2 × 10^5 DLD1 cells were seeded per well of a 6-well plate. The following day, cells were transduced with the lentivius at multiplicity of infection = 1. After 48 h, eGFP-positive cells were sorted using a FACSAria™ II Cell Sorter and cells were seeded again in 6-well plates for assessment of viability over time using the ATPlite assay. For other experiments involving knock-out cell lines, lentivirus was produced and cells were infected and selected as described (Li et al., 2021).

Tumor formation

For *in vivo*-studies, 2.5 × 10^5 DLD1 cells or 1 × 10^6 TSC cells per mouse were mixed 1:1 in Matrigel (Corning) and injected subcutaneously in NSG mice. Tumors were measured three times a week by caliper and tumor volume was calculated using the formula: Tumor volume = width × width × length × 0.52. Treatment with SR-4835 or vehicle was initiated when tumors measured 100 - 150 mm3 and was administered orally 5 days per week at 20 mg/kg prepared in 10/90 DMSO/30% Hydroxypropyl-β-Cyclodextrin in water. If individual tumor volume measurements of replicates from the treatment cohorts were measured on two consecutive days, they were analyzed and plotted together.

Fitness scores and sequencing data from CRC cell line panel

Fitness Scores and DNA alterations of 31 CRC cell lines were obtained from The Cancer Dependency Map at Sanger (accessed via https://score.depmap.sanger.ac.uk and https://cellmodelpassports.sanger.ac.uk). Scores were calculated as described (Behan et al., 2019) and DNA- and RNA-sequencing data generated as detailed in van der Meer et al. (2019). CMS and microsatellite status of CRC cell lines were obtained from Linnekamp et al. (2018).

QUANTIFICATION AND STATISTICAL ANALYSIS

Statistical analyses and graphical presentations were performed using Prism (versions 6 to 9, GraphPad). Statistical assays performed are specified in the Figure legends.